Electronic Supplementary Information

A Microscopically Heterogeneous Colloid Electrolyte of Covalent Organic Nanosheets: Endowing Ultrahigh-Voltage, Low-Temperature Lithium Metal Batteries

Weifeng Zhang,‡[a] Guoxing Jiang,‡[a] Wenwu Zou,‡[a] Xilong Chen,[b] Siyuan Peng,[a] Shengguang Qi,[a] Ren-zong Hu,[b] Huiyu Song,[a] Zhiming Cui,[a] Li Du,[a]* and Zhenxing Liang [a,]*

[a] W. Zhang, G. Jiang, W. Zou, S. Peng, S. Qi, Prof. H. Song, Prof. Z. Cui, Prof. L. Du, Prof. Z. Liang
Guangdong Provincial Key Laboratory of Fuel Cell Technology
School of Chemistry and Chemical Engineering, South China University of Technology
Guangzhou 510640, China
E-mail: duli@scut.edu.cn, zliang@scut.edu.cn

[b] X. Chen, Prof. R. Hu
Guangdong Provincial Key Laboratory of Advanced Energy Storage Materials
School of Materials Science and Engineering, South China University of Technology
Guangzhou 510640, China

‡ These authors contributed equally to this work.

TABLE OF CONTENTS

EXPERIMENTAL SECTIONS

Experimental Section 1 | Materials and electrolytes

Blank electrolyte (BE) was 1.2 M $LiPF_6$ in EC/EMC (w/w, 3:7). BEV was 1.2 M $LiPF_6$ in EC/EMC (w/w, 3:7) with 2 wt% vinylene carbonate (VC). Both BE and BEV were purchased from Nanjing Modges Energy Technology Co., Ltd. TCE was obtained by dispersing TpTta (after the ball-milling process) into BE at a concentration of 0.1 mg mL^{-1} and vigorously stirring for 2 hours. The selection of 0.1 mg mL-1 is aimed at preventing extensive sedimentation of TpTta CON. Monolayer polypropylene separators (PP2500, Celgard), polyvinylidene fluoride (PVDF, MTI Corporation), $LiNi_{0.8}Mn_{0.1}Co_{0.1}O_2$ (NMC811, RONBAY TECHNOLOGY), and 400 μm Li foil (China Energy Lithium Co., Ltd.) were used to assemble 2016-type coin cells.

TpTta CON was prepared according to the reported procedures with slight modifications, as shown in Fig. S9.[1] 1,3,5-triformylphloroglucinol (Tp, 99.3 mg, 0.472 mmol) and dichloromethane (8 mL) were added to a 250 mL flask and sonicated for 10 seconds. Acetonitrile (200 mL) was added to the flask and the resulting solution was stirred at room temperature until Tp was dissolved. 4,4',4''-(1,3,5-triazine-2,4,6-triyl) trianiline (Tta, 167.3 mg, 0.472 mmol) was then added to the flask under an argon atmosphere. $Sc(OTf)_3$ (56 mg, 113.6 μmol) was dissolved in 16 mL of acetonitrile and dropped into the reaction flask within 5 min. The reaction was stirred at room temperature for 20 hours. Finally, 1M NaCl aqueous solution (1.6 mL) was added to the reaction vial to precipitate the nanosheets, and the precipitates were collected via centrifugation and washed thoroughly with acetone, dimethylformamide, and methanol. The powder (yield: 63.7%) was dried at 80 °C under vacuum overnight to give the TpTta CON.

Composite cathodes were fabricated by blading the slurry of active material on carbon-coated Al foil. The slurry was composed of NMC811, PVDF, and super P carbon black with a weight ratio of 90:6:4. The areal mass loading of NMC811 were 3.6 and 20 mg cm^{-2} after being dried overnight at 80 °C. All cathode preparation processes were carried out in an argon-filled glove box.

Experimental Section 2 | Characterizations

The material characterizations of samples were investigated by XRD (Rigaku MiniFlex 600), SEM (Carl Zeiss), XPS (Thermo Fisher Scientific), nitrogen physisorption analyses (Quantachrome), TEM (Talos F200S), and AFM (Bruker Dimension Icon). Fourier transform infrared (FT-IR) spectra were collected in the range of 400–4000 cm^{-1} in transmission mode using a Bruker Tensor 27 FT-IR spectrometer. TOF-SIMS was conducted to analyze the CEI/SEI evolution of cycled electrodes with a TESCAN GAIA3 model 2016 UHR SEM. The cycled electrodes were gently rinsed with EMC three times to remove residual salts and dried in a vacuum chamber before characterization. The preparation and transportation processes of the cycled electrode were all operated in an atmosphere filled with argon. The Raman spectra for electrolytes were collected with an XR2xi analysis (Thermo Fisher Scientific). To avoid contamination of the electrolyte with air, the electrolyte was encapsulated in paraffin-encapsulated capillaries for characterization. The transition metal quantity of the anode was investigated by inductively coupled plasma optical emission spectrometry (iCAP

7200 Duo, Thermo Fisher Scientific).

Experimental Section 3 | Electrochemical measurements

2016-type coin cells were assembled to test the electrochemical performance of electrolytes, and the assembly process was carried out in an argon-filled glove box. Cyclic voltammetry (CV) and linear sweep voltammetry (LSV) were performed on an Autolab (Metrohm, Switzerland). Electrochemical impedance spectroscopy (EIS) was carried out on a PARSTAT3000A-DX (Princeton Applied Research, USA). Galvanostatic charge−discharge test was performed using a Land instrument (LANHE, China).

Chemical stability. The oxidation stability of BE and TCE was measured in a 3-electrode electrolytic tank (work electrode, Pt sheet; reference electrode, Li^0 sheet; counter electrode, Li^0 sheet). LSV was carried out with a scan rate of 1 mV s^{-1} and a voltage window of 2–6.5 V versus Li/Li^+.

3-electrode EIS. To eliminate the mutual impact between the cathode/electrolyte impedance and the anode/electrolyte impedance, a 3-electrode setup was applied to study the change process of the interface impedance. The NMC811 cathode served as the work electrode in the 3-electrode setup, while the Li^0 sheet served as the counter electrode and Cu silk served as the reference electrode. The impedance spectrum of 3-electrode cells was collected after 30 cycles at C/3, and the detailed frequency range was 10^5–0.1 Hz.

Galvanostatic charge−discharge test. For Li|NMC811 cells, activated cycling (first two cycles) with a current rate of 0.2C and a voltage window of 2.8–4.3 V versus Li/Li^+ was performed to form an inorganic-rich interphase. Subsequent galvanostatic charge−discharge tests were conducted at a current rate of C/3 and a voltage window of 2.8–4.7 V or 2.8–4.6 V versus Li/Li^+, unless otherwise specified.

Other. A frequency range of 10^5–0.1 Hz was used for temperature-dependent EIS experiments, which were carried out at 293.15 K, 298.15 K, 303.15 K, and 313.15 K. A constant current rate of 0.1C with a duration of 600 s, a cut-off voltage of 4.7 V versus Li/Li^+, and a subsequent 3600 s open-circuit stand were applied to accomplish the galvanostatic intermittent titration technique (GITT) measurement. A scan rate of 0.001 V s^{-1} and a voltage window of –0.15 to 0.15 V versus Li/Li^+ in LSV were considered to extract exchange current density. The CV parameters of Li|NMC811 cells (including different scan rates and multiple cycles) can be inferred from the annotations in the figure.

Experimental Section 4 | MD simulations

All molecular dynamics simulations were carried out by Gromacs2019.6.[2] Initial simulation systems were constructed by uniformly mixing 221 Li^+, 221 PF_6^- with 681 EC molecules and 1345 EMC molecules to form the electrolyte phase. Three TpTta layers with a spacing of ~3.4 Å were placed in the box center area. The box size was 6.4 nm and 5.5 nm in x-y dimensions, respectively, while the z-dimension was 9.6 nm with TpTta and 9.0 nm without TpTta, respectively. Parameters of Li^+ were obtained from the amber force field, other species, including TpTta, EC, EMC, and PF_6^-, were all parameterized by the general amber force field.[3] The vdW interactions were described by Lennard Jones (LJ) potential, with LJ parameters between unlike atom-pairs automatically determinzed by Lorentz-Berthelot mixing rules. The cut-off distance for the vdW interactions was set at 1.2 nm. Coulombic interactions were computed with the PME method. Energy-minimization was first conducted to relax the initial configurations, then 10-ns production runs were carried out at 298.15 K and 1 bar. A time step of 1 fs was used. Equations of motion were integrated by the leapfrog

algorithm. Three-dimensional periodic boundary conditions were applied during simulations.

Experimental Section 5 | DFT calculations

For all DFT calculations, Materials Studio's Dmol3 module with the functional GGA-PBE was employed.[4-6] The energy convergence criterion of 1×10^{-5} Ha and the force convergence criterion of 0.02 Ha/Å were set during all calculations. The Brillouin zone was sampled with Gamma point for COF unit cell optimization. The Grimme method for DFT-D correction was incorporated to describe the van der Waals interactions.[7] In addition, the optimized supercell of COF with a vacuum space of 15 Å was estimated with an implicit solvent model utilizing the DFT-COSMO for the desolvation energy calculation.[8, 9] A typical mixed solvent electrolyte environment was represented using the COSMO implicit solvation model with acetone parameters (with a dielectric constant of 20.7).

SUPPLEMENTARY NOTES

Note S1 | Additional discussion of MD simulations

The MD simulation of TCE is mainly divided into two parts, that is, the statistical analysis of the Li^+ solvation environment is divided into TCE-adjacent to TpTta and TCE-away from TpTta. Top-view snapshots of MD simulation are shown in Fig. S1. The Li^+ solvation structure away from TpTta is highly similar to that in BE (Fig. 2b and Fig. S4). However, the Li^+ solvation structure closed to TpTta is quite different from that in BE, and the solvent-separated ion pair (SSIP) is dominant in both BE and TCE-away from TpTta. The coordinated solvent in the SSIP will preferentially form a thick, organic-rich SEI at the Li^0/electrolyte interface because of the lower lowest unoccupied molecular orbital (LUMO) energy.[10] This will cause the impedance to rapidly increase, especially in low-temperature environments (the Li^0/electrolyte interface's impedance predominates the cell's overall impedance).[11]

Note S2 | TpTta for Li^+ desolvation

Due to its smaller radius, Li^+ coordinates with solvent molecules in the electrolyte.[12] Ethylene carbonate (EC) exhibits remarkable advantages as a coordinating solvent for Li^+ due to its exceptionally high dielectric constant of 90.8, with the primary coordination species being $Li(EC)_4^+$ (Nonaqueous Liquid Electrolytes for Lithium-Based Rechargeable Batteries). The dissociation energy required for $Li(EC)_4^+$ to dissociate into $Li(EC)_3^+$ and one EC molecule in the routine electrolyte was approximately 52.5 kJ mol^{-1} (Fig. S7). Based on the electrostatic potential map, it is evident that the tails of the bottom three EC molecules in $Li(EC)_4^+$ carry a positive charge, resulting in a strong electrostatic attraction with the triazine group (negative charge) on TpTta (Fig. S8a-b). Next, the upper EC molecules in $Li(EC)_4^+$ can be readily dissociated with a dissociation energy of 45.5 kJ mol^{-1}, much lower than that in routine electrolytes (Fig. S8c).

Note S3 | Discussion of TpTta synthesis

The Fourier transform infrared (FT-IR) spectrum of TpTta CON shows a distinct peak at 1575 cm^{-1} for the C=C stretching merged with a sharp peak at 1269 cm^{-1} for the C–N stretching (Fig. S10).[13] This indicates that the aldehyde group in 1,3,5-triformylphloroglucinol (Tp) and the amino group in 4,4',4"-(1,3,5-triazine-2,4,6-triyl) trianiline (Tta) have been successfully condensed and have undergone the irreversible reaction of the enol-to-keto tautomerism to generate the expected framework with C–N linkage.[14, 15] To confirm the successful synthesis of TpTta CON, X-ray photoelectron spectroscopy (XPS) was employed. Fig. S11 displays a comprehensive analysis of the C 1s peak. The peaks observed at 290.6 eV, 286.8 eV, 285.9 eV, and 284.7 eV correspond to the C=O, C=N, C−N, and C=C/C−C functionalities within the TpTta CON structure. PXRD and HR-TEM were used to characterize the ordered framework of TpTta CON (Fig. S12). The powder X-ray diffraction (PXRD) pattern shows an intense peak at 5.6° and a minor peak at 9.9°, corresponding to (100) and (110). The major broad peak at 26.5°, corresponding to the (001) reflection plane, signifies poor π-π stacking between the vertically stacked layers.[16, 17] Even so, distinct lattice fringes could be observed in the HR-TEM image of TpTta CON, which illustrates the structurally ordered nature of the nanosheets. The low crystallinity of TpTta CON is attributed to the random stacking of nanosheets, which favors fast ion transport through the effective elimination of grain boundaries.[16, 18-20] N_2 adsorption and desorption curves were used to analyze the porosity of TpTta CON (Fig. S13). The Brunauer−Emmett−Teller (BET) surface area and pore diameter of TpTta CON were calculated to be 56.1 m^2 g^{-1} and 1.48 nm. The small surface area of TpTta CON may be due to poor layer stacking and random alignment of nanosheets.[16, 17] In addition, the pore diameter

calculated on the basis of nonlocal density function theory (NLDFT) is ~1.44 nm, which is consistent with the theoretical simulations.

Note S4 | Raman spectra and coordination analysis of PF_6^-

Raman spectroscopy can clearly investigate the coordination between PF_6^- and other molecules in different electrolytes (Fig. S16a). There was no significant difference in the peak attributed to coordinated PF_6^- in BE and BEV. However, TpTta can enhance the formation of contact ion pairs (CIP) and cation-anion aggregates (AGGs), causing the peak of coordinated PF_6^- at 740.1 cm^{-1} shift to 741.9 cm^{-1} (Fig. S16b). The peak shift may be attributed to the following reasons: the co-adsorption effect of TpTta to Li^+ and PF_6^- changes their coordination environment (Fig. S16c). By increasing the proportion of anions surrounding the Li^+, the cation−anion interactions were enhanced, which is consistent with the MD results.

Note S5 | Additional discussion of three-electrode cells for EIS

The interface impedances of cathode/electrolyte and anode/electrolyte are both included in the overall resistances determined by the conventional two-electrode cell. It is difficult to extract the contribution of each electrode interface to the impedance of the whole battery, especially for the interface engineering of the electrolyte. Since the three-electrode cell introduces another reference electrode instead of directly using the Li^0 anode as a reference electrode, the impedance evolution of each electrode interface can be investigated in detail. Specifically, the three-electrode cell used NMC811 as the working electrode, Li^0 as the counter electrode, and Cu wire-connected Li^0 wire as the reference electrode (Fig. S23a).

The Nyquist curves of the cathode part and the anode part are respectively fitted through the equivalent circuit in Fig. S23b-c. The main rules in the fitting results include: a) In RT operation, the impedance of the cathode side is the dominant factor in the overall impedance. In contrast, at −20°C operation, the anode side impedance is the dominant factor in the overall impedance. b) Compared with BE, the introduction of TpTta in TCE can greatly reduce the impedance of Li^+ de-solvation and passing through interphase, especially the latter (Fig. 3e and Table S3).

Note S6 | TCE for inhibiting side reaction of Li|NMC811 cells

To understand the electrochemical activity of TpTta in TCE and its effect on interface evolution, multiple-cycle CV scans were conducted with Li|NMC811 cells. The phase transition during charging follows H1-M-H2 (<4.1 V versus Li/Li^+) and H2-H3a (>4.1 V versus Li/Li^+), which is similar to the reported literature. In detail, the oxidation at ~3.79 V versus Li/Li^+ contributes to the main charging capacity, which is also closely related to the charging performance of the cell. It can be seen from Fig. S25 that the oxidation potential of Li|NMC811 cells cycled in BE and BEV increases gradually with the increase in cycle number and reaches 3.79 V versus Li/Li^+ at the 10^{th} cycle, which may be due to the slow kinetics of Li^+ deintercalation in the cathode and the increasing electrode/electrolyte interface impedance. During the reduction process, the reduction potential of cells cycled in BE as well as in BEV decreased continuously, indicating the degradation of the interface. A higher reduction potential indicates better electrochemical performance. In stark contrast to BE and BEV, the cell cycled in TCE reached the lowest oxidation potential of 3.75 V versus Li/Li^+ and the highest reduction potential of 4.18 V versus Li/Li^+ at the 10^{th} cycle. The better electrochemical performance of Li|NMC811 cells cycled in TCE can be attributed to the fact that PF_6^--derived LiF-rich CEI/SEI can effectively suppress the undesirable evolution of the interface, accelerate the Li^+ intercalation/deintercalation in the cathode and the Li^0 stripping/plating in the anode.

To further investigate the degradation degree of NMC811 cathode at ultra-high cut-off voltages, accelerated degradation tests at 4.7 V versus Li/Li^+ were performed (Fig. S25d). In BE and BEV, the leakage current densities are 9.9 μA mg^{-1} and 9.2 μA mg^{-1}, respectively. A higher leakage current density means more severe interfacial side reactions. In contrast, the leakage current density in TCE is only 7.4 μA mg^{-1}, which indicates that the NMC811 cathode cycled in TCE can form an effective passivation layer against interfacial side reactions at high oxidation potential.

Note S7 | TCE for suppressing phase reconstruction of NMC811

When the NMC811 cathode was charged from the open circuit voltage to 4.0 V versus Li/Li^+, the phase transition H1-M-H2 occurred. When the cut-off voltage was increased to 4.1 V versus Li/Li^+, the phase transition H2-H3a occurred. In the H2-H3a phase transition, the anisotropic shrinkage caused by the slight shrinkage of the *a*-axis and the severe shrinkage of the *c*-axis will cause structural integrity and obvious particle cracks.[21] The lattice mismatch caused by serious multiple-phase transitions will aggravate the dissolution of transition metals. As demonstrated in Fig. S26-27, the cycled NMC811 particle in TCE did not show obvious cracks, and the Li^0 anode also showed a lower concentration of transition metals, which makes a strong contrast with the control sample. The above results can be attributed to the fact that the LiF-rich CEI on the particle surface inhibits the dissolution of transition metals and suppresses the irreversible structural decay of the NMC811 cathode.

In the H1-M-H2 phase transition, because the *a*-axis of the first hexagonal phase (H1) and the second hexagonal phase (H2) were far apart from the *b*-axis of the monoclinic phase (M) when the two phases coexisted, the (101) peak displayed a distinct split throughout this process. The subsequent multiple-phase transitions cause the deformation of crystal structure and the accumulation of strain, resulting in the splitting of the (101) peak after discharge to 2.8 V versus Li/Li^+ (Fig. S28).[22]

Note S8 | TCE for Li^+ diffusion in NMC811

The CV with different scan rates was used to study the effect of TpTta on the Li^+ diffusion efficiency in the cathode (Fig. S29). The Li^+ diffusion coefficient (D_{Li^+}) in different phase transitions can be extracted from the relationship between the peak current (i_p) and the square root of the scan rate ($v^{1/2}$) in the Randles–Sevcik equation (1):

$$i_p = 2.69 \times 10^5 n^{3/2} A C_0 D_{Li^+}^{1/2} v^{1/2} \quad (1)$$

The galvanostatic intermittent titration technique (GITT) can investigate the mechanism of electrode degradation and the characteristics of the electrode/electrolyte interface. As shown in Fig. S30, the voltage drops and polarization voltage of the cells cycled in TCE are smaller than those cycled in BE and BEV, which highlights the advantages of TCE.

Note S9 | Outlook on CON Colloid Electrolytes

This study introduces the groundbreaking concept of microscopic heterogeneous electrolyte (CON colloid electrolyte) and applies them to LMBs with nickel-rich layered cathode materials. The CON colloid electrolyte showcases remarkable outlooks, as follows:

First of all, mesoscopic CON stands for a crystalline porous polymeric material covalently bonded from organic monomers, offering outstanding physical and chemical stability, a diverse range of functional groups, open and ordered channels, adjustable structures, and ease of customization. In practical applications, tailored functionalities and charge properties can be introduced by designing specific organic monomers or connection

bonds, endowing CON with unique capabilities. Especially for complex electrolyte systems, there are many issues to address, and existing electrolytes have failed to address their multifaceted problems. Although the colloid electrolyte design principle has been proposed for application in the field of batteries, it is still challenging for a dispersoid with single functionality to simultaneously resolve various issues within the electrolyte system. In this study, we carefully selected functional groups in CON and synthesized thin-layered TpTta (with a thickness of < 1.25 nm and a lateral size of < 100 nm) using suitable synthesis methods. By incorporating TpTta, which demonstrates a co-adsorption effect, into commercial electrolytes, we successfully achieved excellent electrochemical performance for batteries, even under ultra-high voltage and low-temperature conditions. Although our focus was on TpTta in this work, the tunable property of CON suggests that by rationally selecting CON's functional groups, other CON variants with meso-micro multiscale interaction can be developed to enhance mass transfer and electrochemical activity at the electrode/electrolyte interface of other alkali-ion/metal batteries.

Secondly, CON dispersed within the electrolyte displays robust chemical stability, a clear departure from conventional electrolyte additives. Most of the reported electrolyte additives are mostly self-sacrificing additives; that is, a good electrode/electrolyte interface is formed through the decomposition of additives, which makes it difficult to ensure the long life of batteries. In contrast, by rationally manipulating CON's structure and synthesizing chemically or physically stable CON, exceptional electrochemical performance and enhanced stability can be achieved simultaneously.

Finally, the CON colloid electrolyte has the distinct advantage of no longer relying on high-concentration Li salts and novel solvents, substantially easing the complexity and cost of synthesizing high-performance electrolytes. Conventional electrolyte strategies, including HCE and LHCE, are reliant on expensive Li salts or diluents, leading to concerns about industrial feasibility. While the organic monomers used to synthesize CON may not be low-cost, the minimal dosage of CON in the colloid electrolyte (only 0.1 mg mL^{-1} in this study) substantially reduces costs compared to battery-grade additives, Li salts, and solvents. For instance, when considering equivalent volumes ($\rho \approx 1.2$ g mL^{-1}), the mass of VC in BEV is 240 times greater than that of TpTta in TCE, highlighting the cost-effective characteristic of the CON colloid electrolyte design. By dispersing such a minimal dosage of CON in commercial electrolytes, the colloid electrolyte successfully achieves outstanding electrochemical performance compared to state-of-art electrolytes. Consequently, with cost considerations in mind, the colloid electrolyte holds a promising outlook for industrial applications.

SUPPLEMENTARY FIGURES

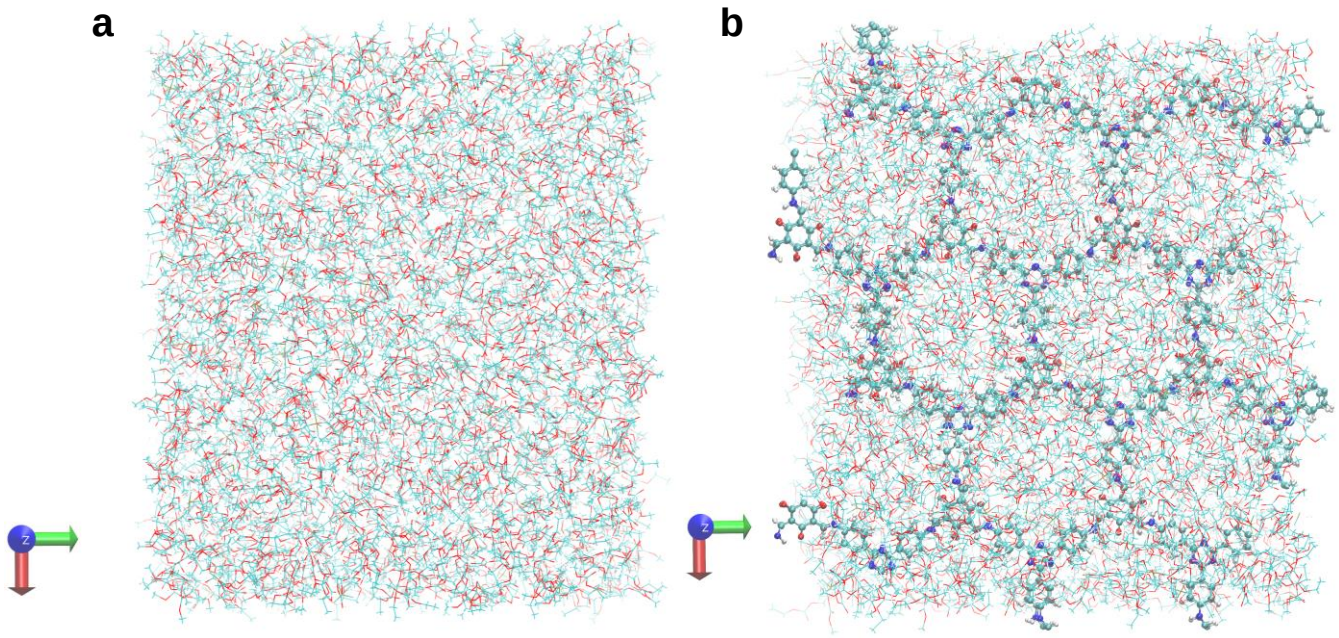

Fig. S1. Top-view snapshot of MD simulations of (a) BE and (b) TCE. Colour schemes are used: *x* axis, red; *y* axis, green; *z* axis, blue.

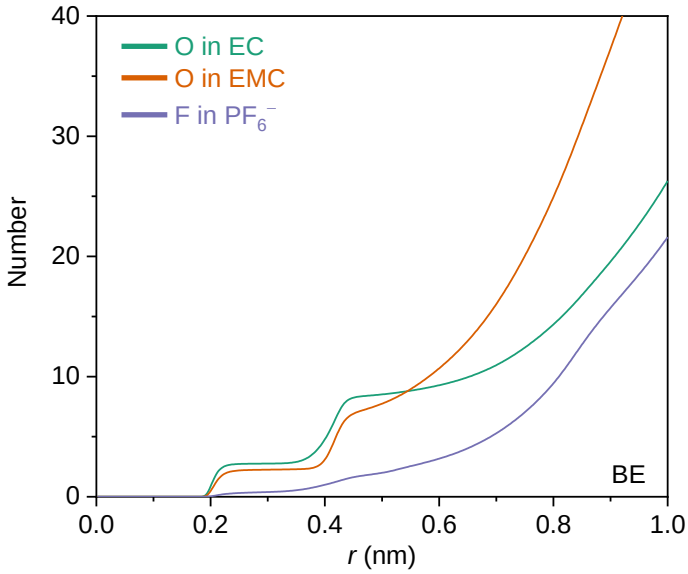

Fig. S2. Coordination number of EC, EMC, PF_6^- with respect to Li^+ in BE.

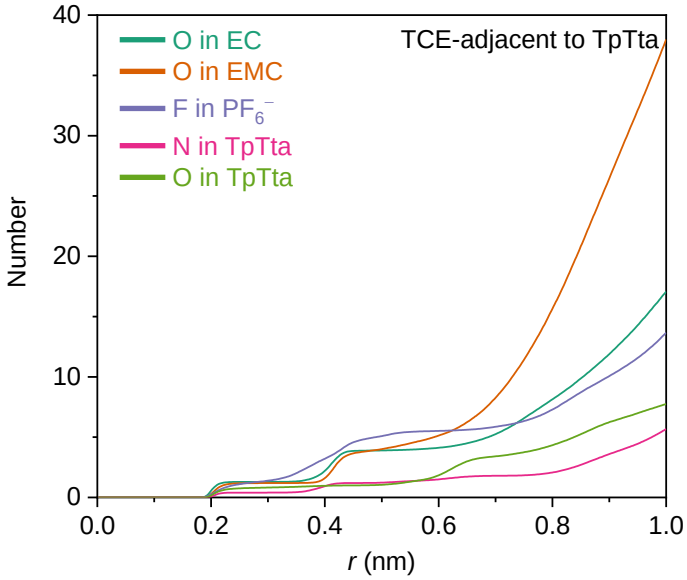

Fig. S3. Coordination number of EC, EMC, PF_6^- with respect to Li^+ in TCE (adjacent to TpTta).

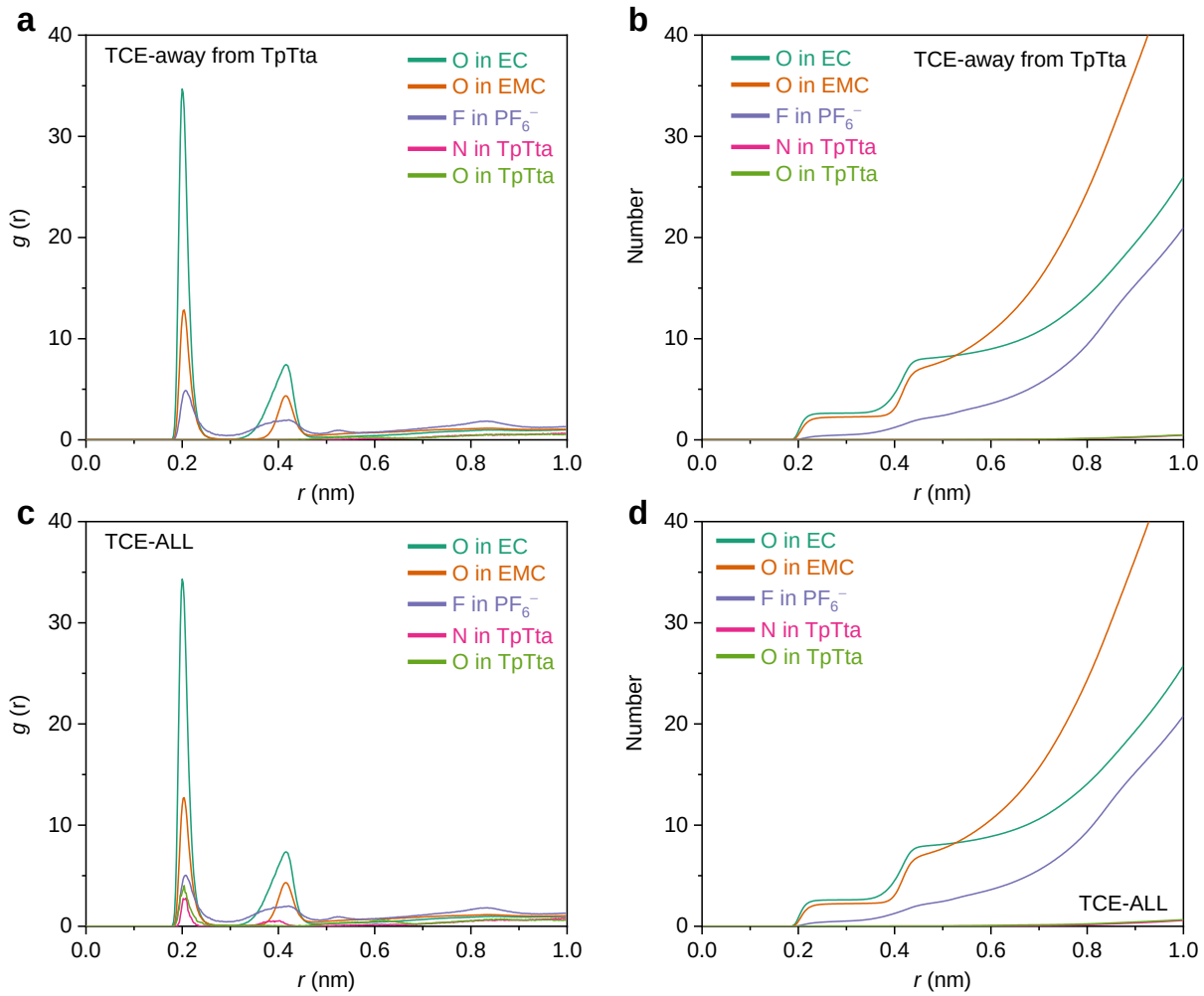

Fig. S4. (a) Radial distribution functions and corresponding (b) coordination number of EC, EMC, PF_6^-, and TpTta with respect to Li^+ in TCE (away from TpTta). (c) Radial distribution functions and corresponding (d) coordination number of EC, EMC, PF_6^-, and TpTta with respect to Li^+ in TCE (whole system).

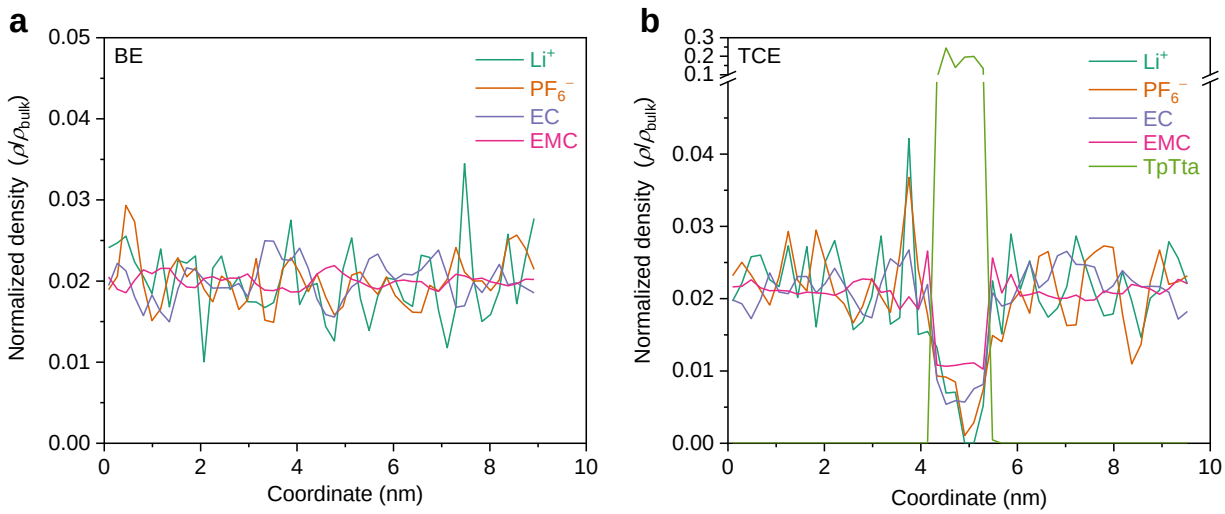

Fig. S5. Density profiles of (a) BE and (b) TCE. ρ and ρ_{bulk} represent the amount and the total amount of specified species, respectively.

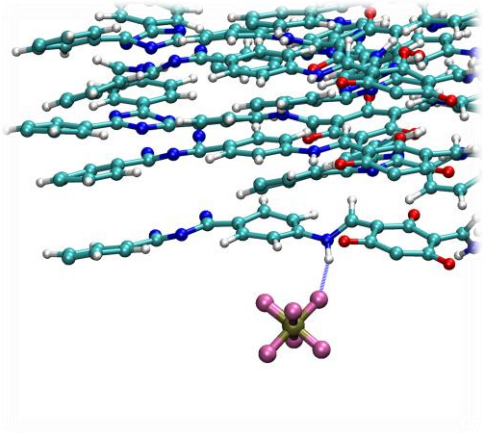

Fig. S6. Representative hydrogen bond between PF_6^- and TpTta.

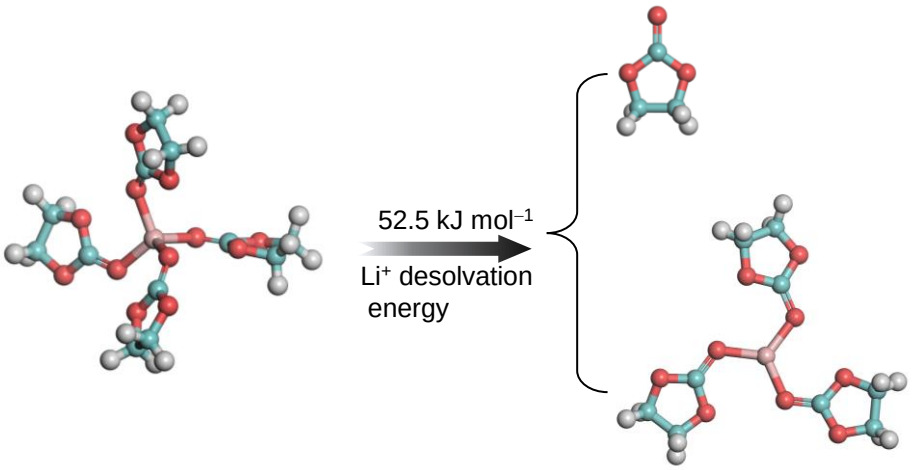

Fig. S7. Li^+ de-solvation process ($Li(EC)_4^+$ to $Li(EC)_3^+$ and EC molecule) in BE. Colour schemes are used: Li, pink; C, cyan; O, red; H, grey.

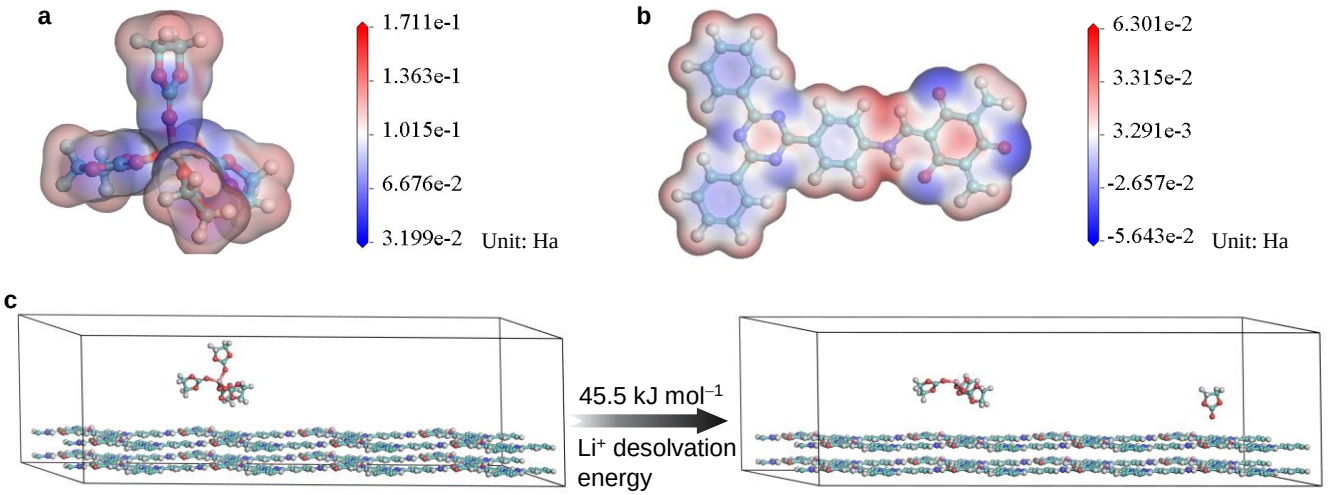

Fig. S8. Electrostatic potential map of (a) $Li(EC)_4^+$ and (b) TpTta. (c) Li^+ de-solvation process ($Li(EC)_4^+$ to $Li(EC)_3^+$ and EC molecule) in TCE. Colour schemes are used: Li, pink; C, cyan; O, red; H, grey; N, blue.

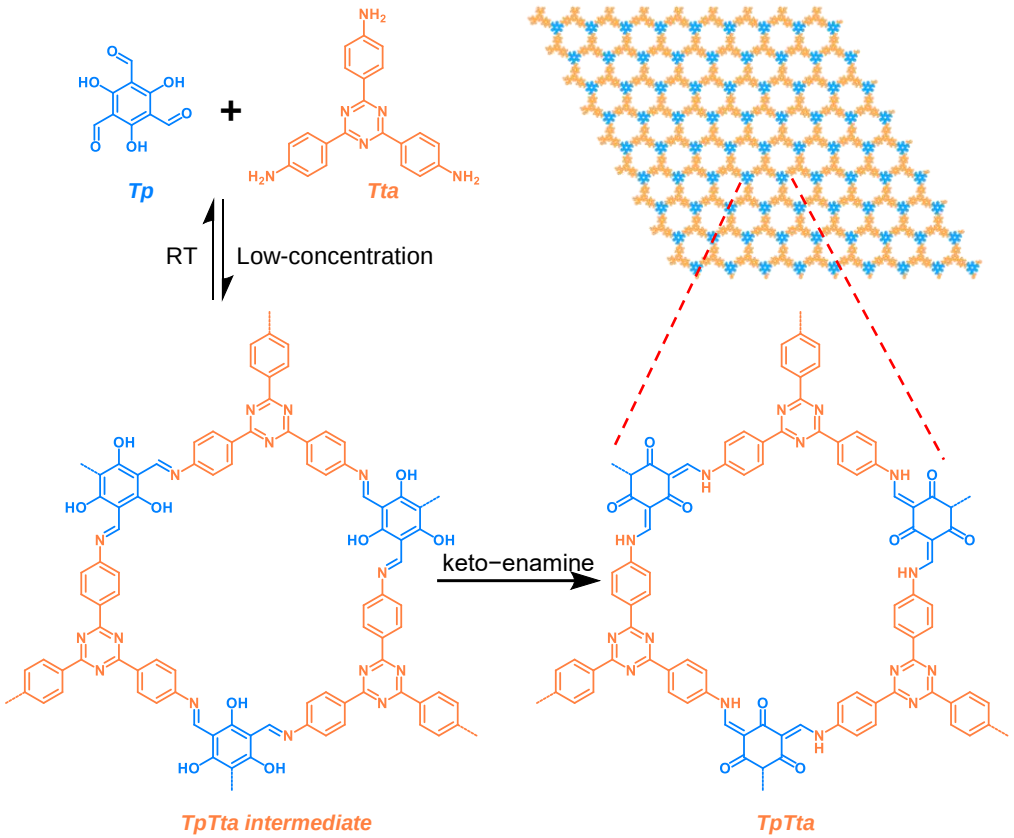

Fig. S9. Synthetic scheme of the TpTta CON via solution-processed strategy at room temperature.

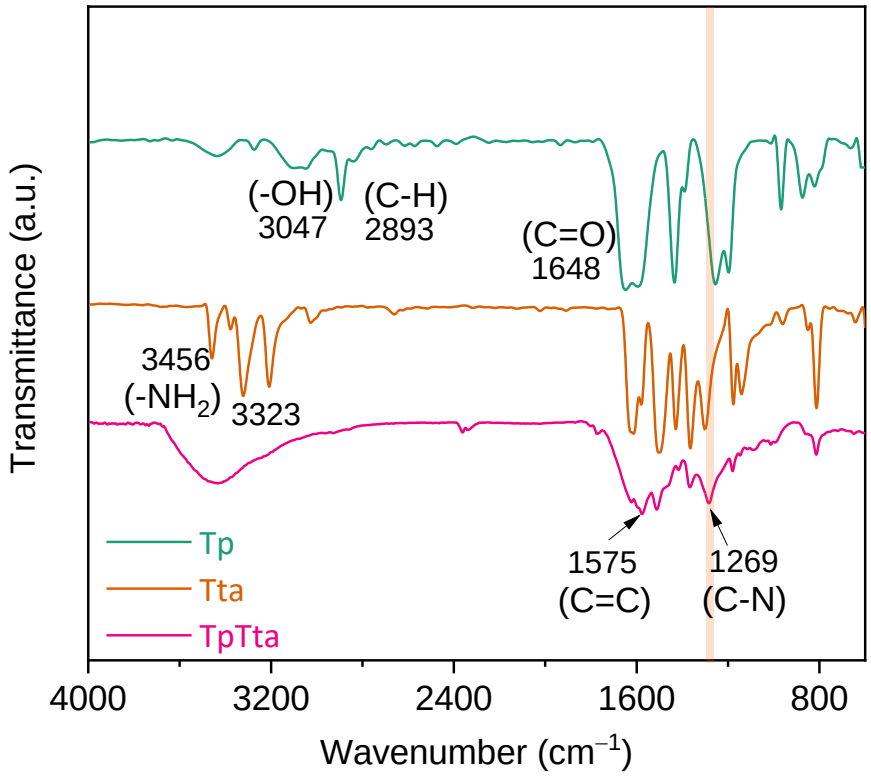

Fig. S10. Fourier transform infrared spectrum (FT-IR) of TpTta CON.

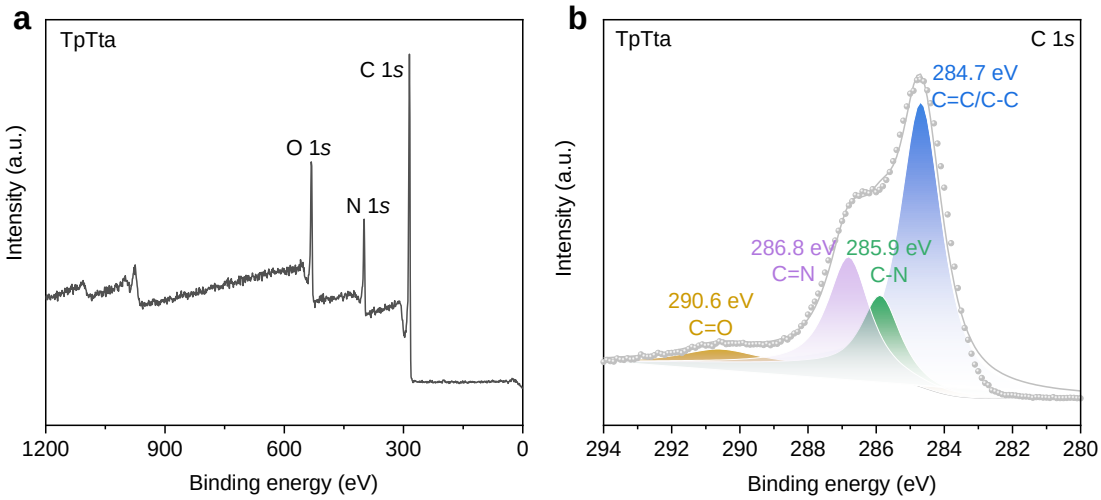

Fig. S11. (a) XPS profiles of TpTta CON. (b) C 1*s* patterns of TpTta CON.

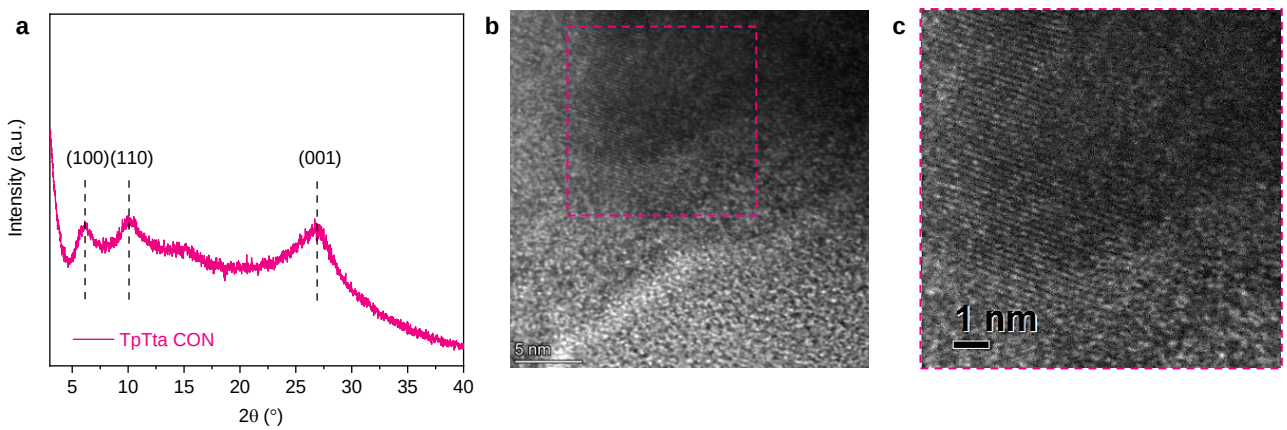

Fig. S12. (a) Powder X-ray Diffraction (PXRD) of TpTta CON. (b-c) Transmission electron microscope (TEM) of TpTta CON.

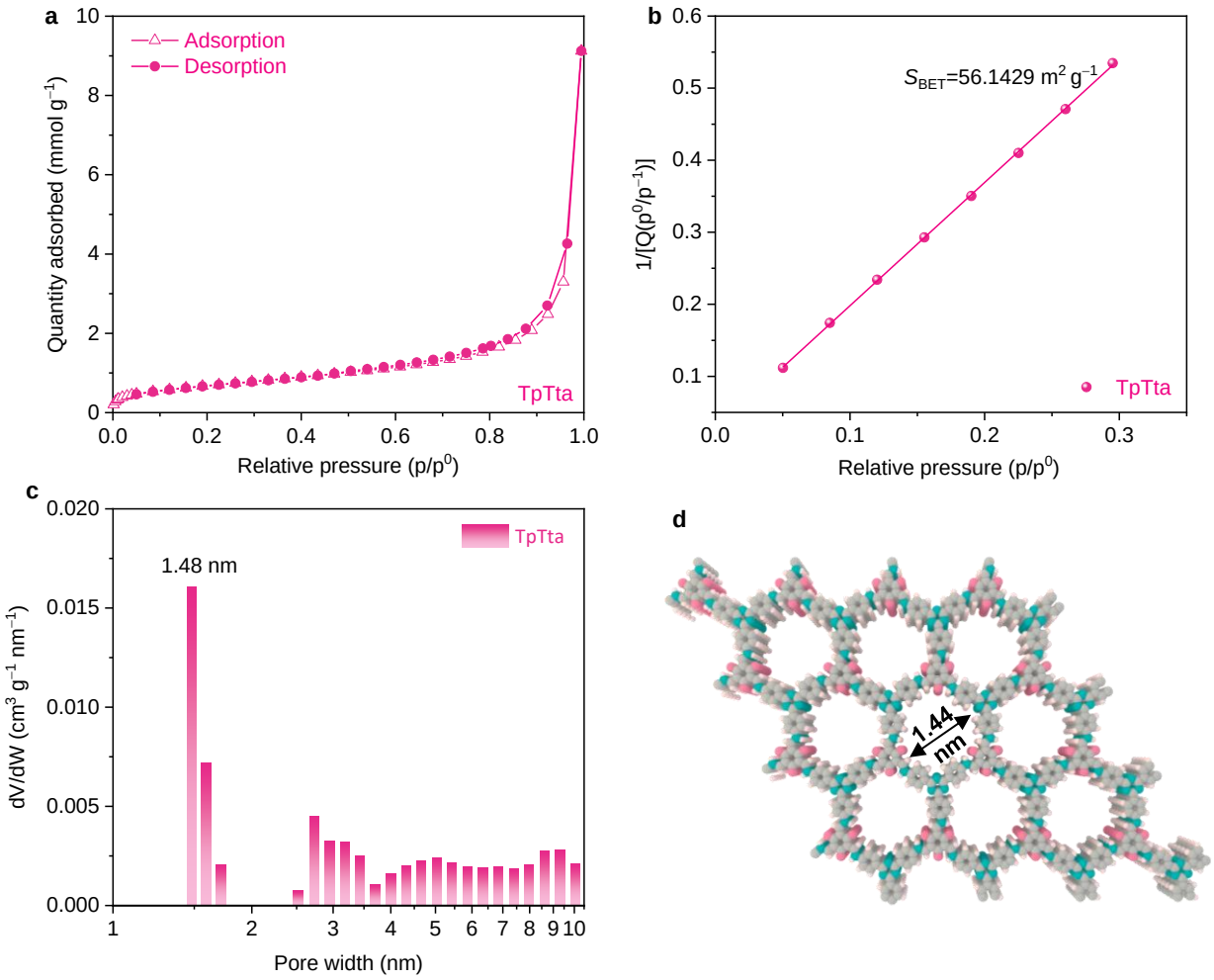

Fig. S13. (a) N_2 adsorption isotherm, (b) specific surface area, and (c) pore size distributions of TpTta CON. (d) The calculated pore size of the TpTta is 1.44 nm, which is close to the measured pore size of 1.48 nm. The specific surface area of TpTta is 56.1429 m^2 g^{-1}, significantly lower than those reported in existing literature[23, 24]. This is attributed to the room temperature synthesis method employed in this study to prepare TpTta CON, aiming to achieve excellent dispersibility of nanosheets, as opposed to the conventional solvent-thermal method.

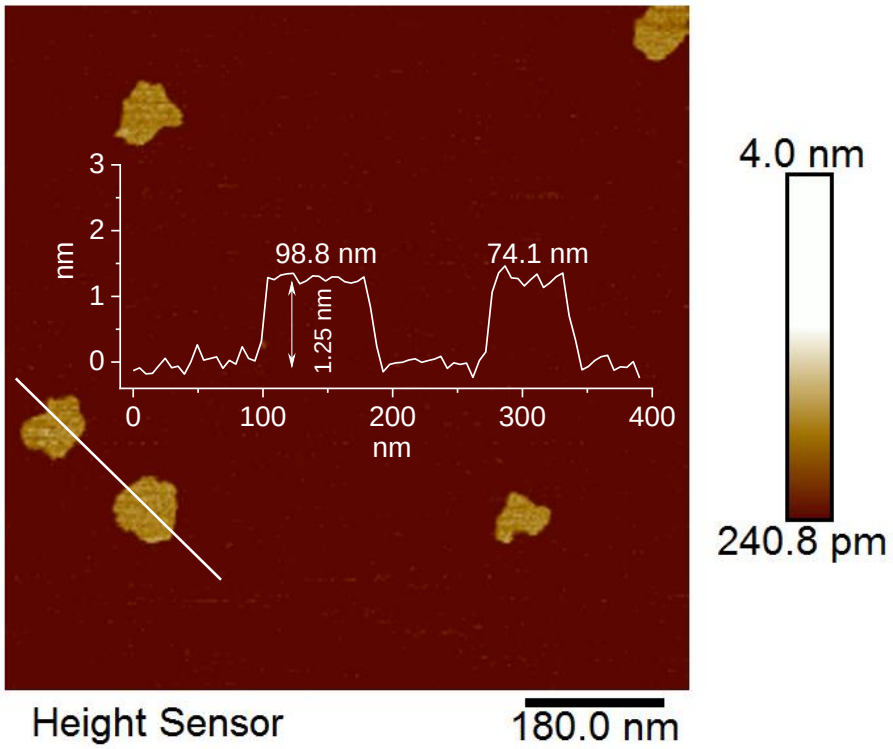

Fig. S14. Atomic force microscopy (AFM) of TpTta CON (insert: height profiles of representative nanosheet). The thickness of TpTta CON was determined through atomic force microscopy (AFM). The lateral dimension and vertical thickness of TpTta CON were found to be under 100 and 1.25 nm, respectively. The longitudinal thickness of TpTta CON, which is less than 100 nm, proves advantageous for crafting colloidal electrolytes characterized by robust physical stability. The ultrathin CON thickness facilitates the exposure of additional sites for ion adsorption.

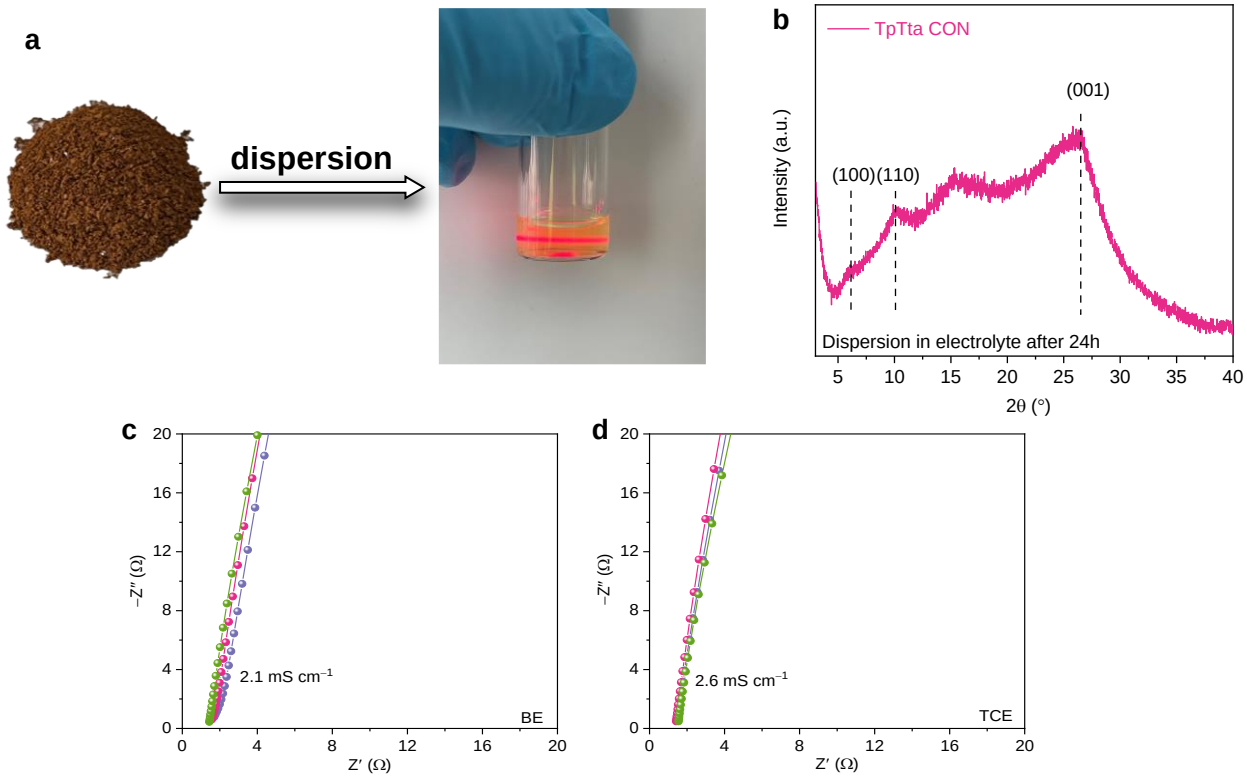

Fig. S15. (a) Optical photograph of TpTta CON powder and TCE. Dispersion of TpTta CON into the blank electrolyte (1.2 M $LiPF_6$ in EC/EMC) showed Tyndall effect, which indicated that the dispersion was colloid. (b) PXRD of TpTta CON (dispersion in electrolyte after 24h). Diffraction peaks corresponding to pristine TpTta CON (including 100, 110, and 001 plane) were observed after dispersion, indicating the stability of TpTta in the electrolyte. Ionic conductivity of the (c) BE and (d) TCE at RT. In addition, the incorporation of TpTta CON did not decrease the Li^+ conductivity of the electrolyte.

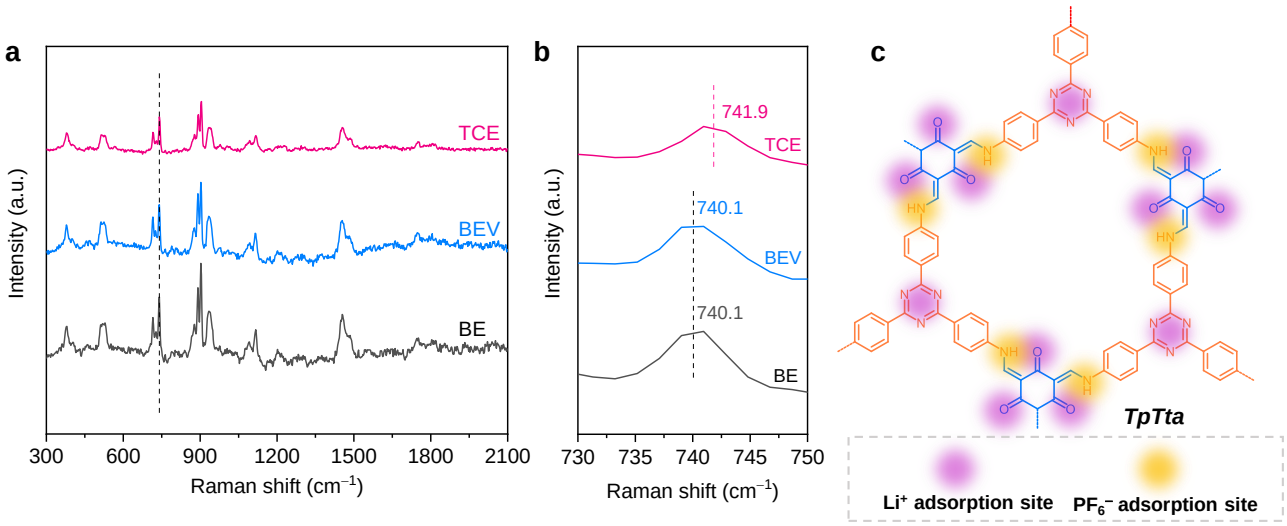

Fig. S16. (a) Raman spectra and the (b) magnified local profiles of different electrolyte. (c) Schematic illustration of the co-adsorption effect of TpTta.

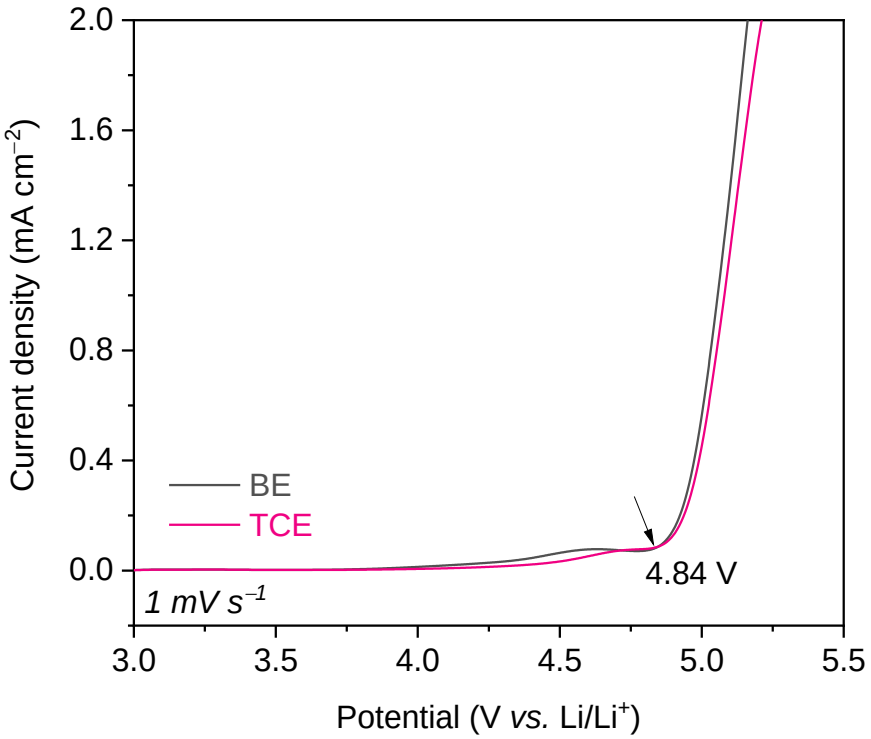

Fig. S17. LSVs of different electrolyte in three-electrode set up cell (work electrode: Pt, reference electrode: Li^0 plate, counter electrode: Li^0 plate). At room temperature, the anodic stability of TCE was evaluated using platinum (Pt) as the working electrode through LSV measurements. Both TCE and BE demonstrated significant oxidation potentials at 4.84 V versus Li/Li^+, which indicated that TpTta would not be oxidized below 4.84 V versus Li/Li^+.

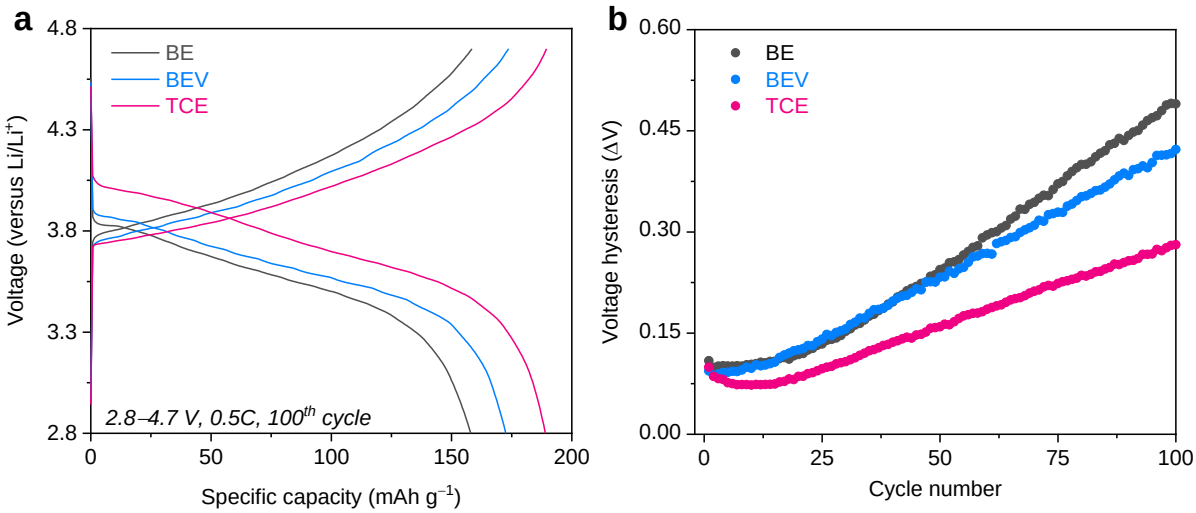

Fig. S18. (a) Charge–discharge profiles of the 100th cycle within 2.8–4.7 V. (b) Hysteresis voltage of Li|NMC811 cells at 0.5C between 2.8 and 4.7 V at RT.

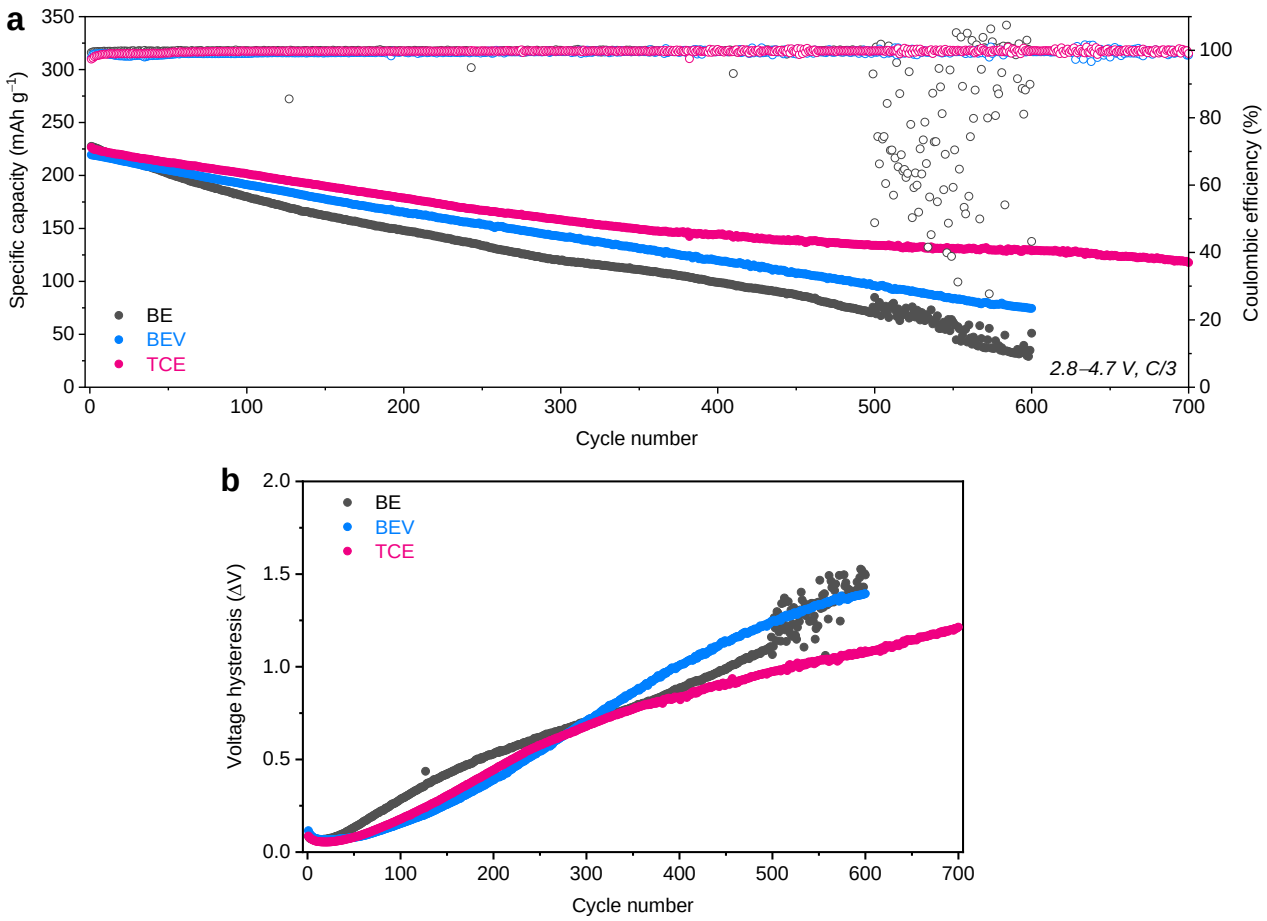

Fig. S19. (a) Cycling performance and corresponding (b) hysteresis voltage of Li|NMC811 cells at C/3 between 2.8 V and 4.7 V under RT.

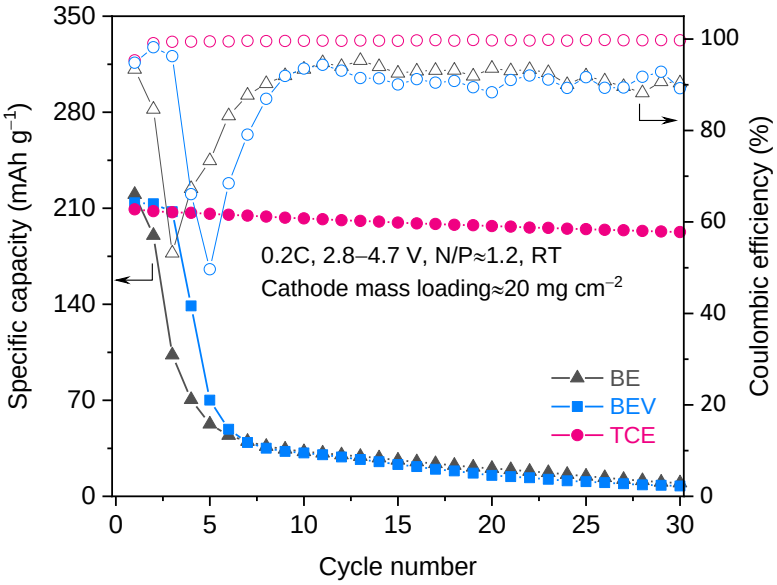

Fig. S20. Cycling performance of Li|NMC811 cells with a high cathode mass loading of ~20 mg cm^{-2} at 0.2C between 2.8 V and 4.7 V under RT.

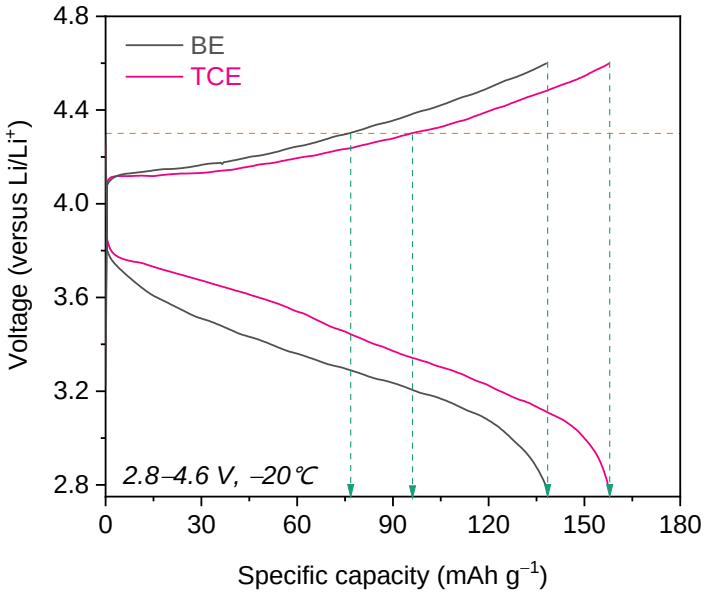

Fig. S21. Representative charge–discharge profiles of Li|NMC811 cells from selected cycles within 2.8–4.6 V at –20℃.

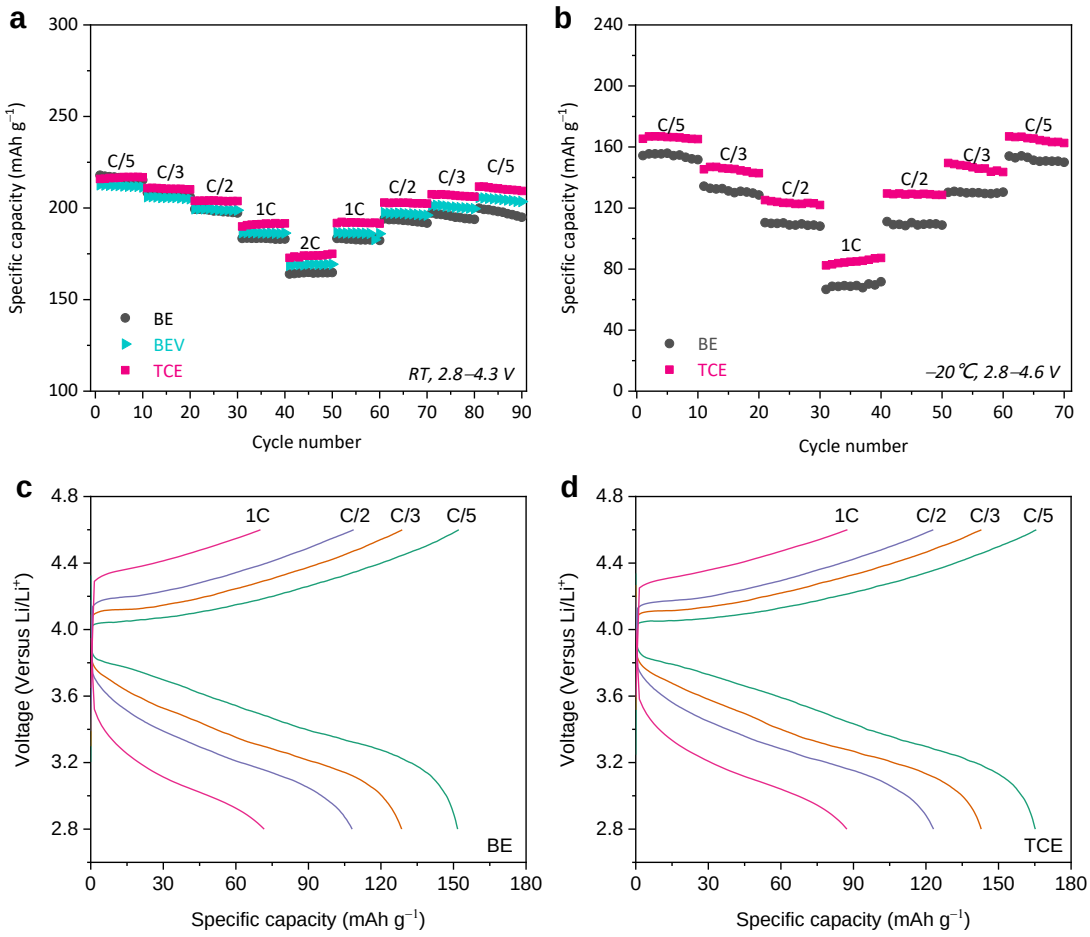

Fig. S22. (a) C-Rate performance of Li|NMC811 cells between 2.8 V and 4.3 V under RT. (b) C-Rate performance of Li|NMC811 cells between 2.8 V and 4.6 V under –20°C. Representative charge–discharge profiles of C-rate performance of Li|NMC811 cells with (c) BE and (d) TCE under –20°C.

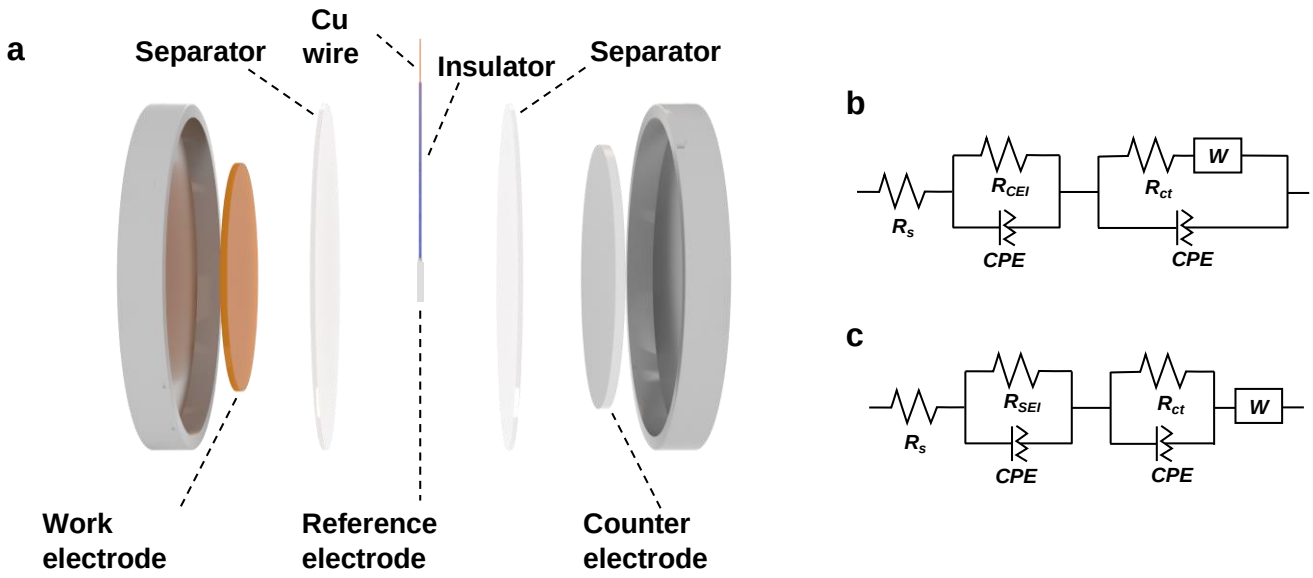

Fig. S23. (a) Schematic illustration of three-electrode set up NMC811 cells for EIS test. Equivalent circuit for EIS modelling at (b) cathode side and (c) anode side.

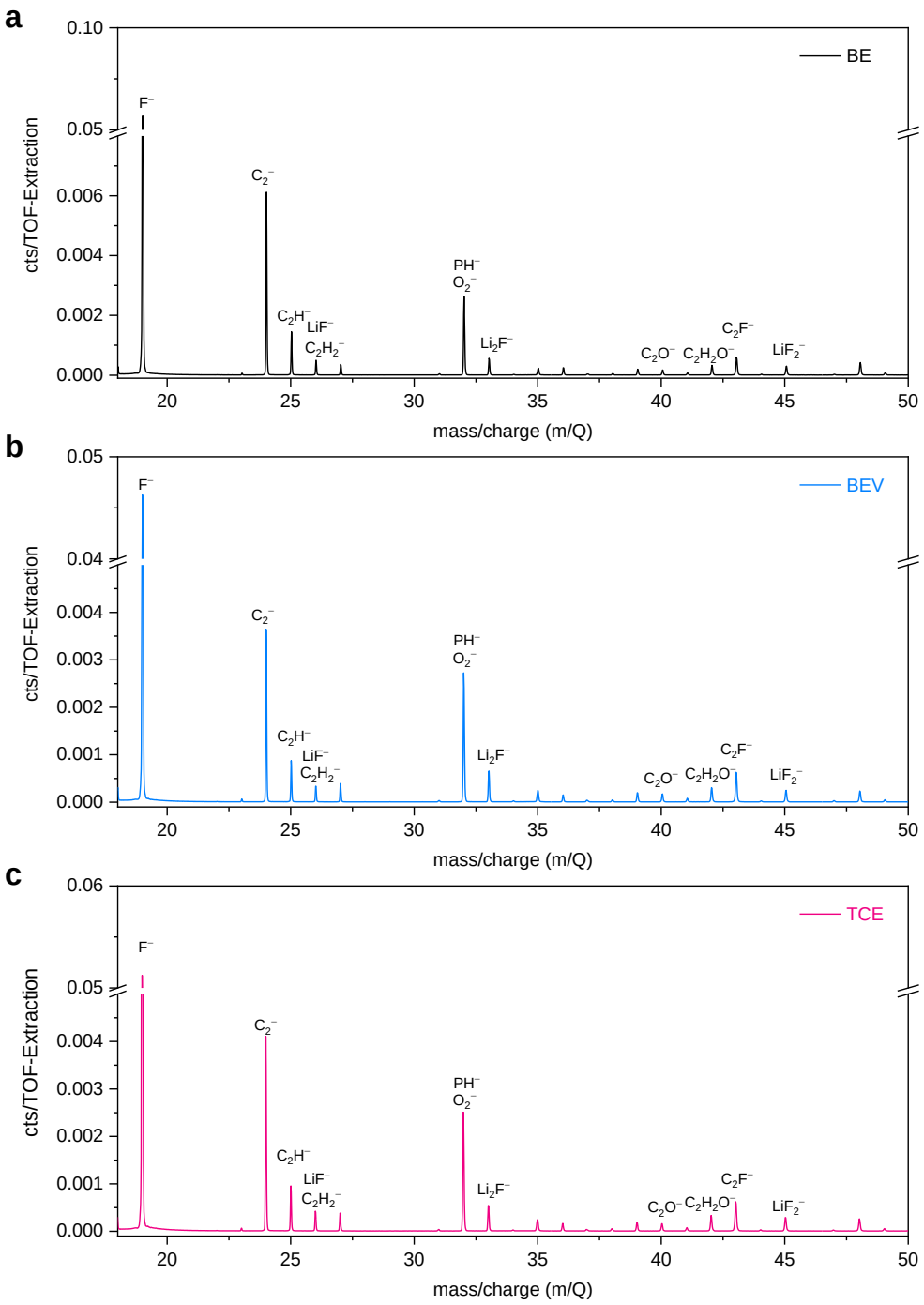

Fig. S24. Ex situ TOF-SIMS analysis of NMC811 cathodes retrieved from Li|NMC811 cells with (a) BE, (b) BEV, and (c) TCE.

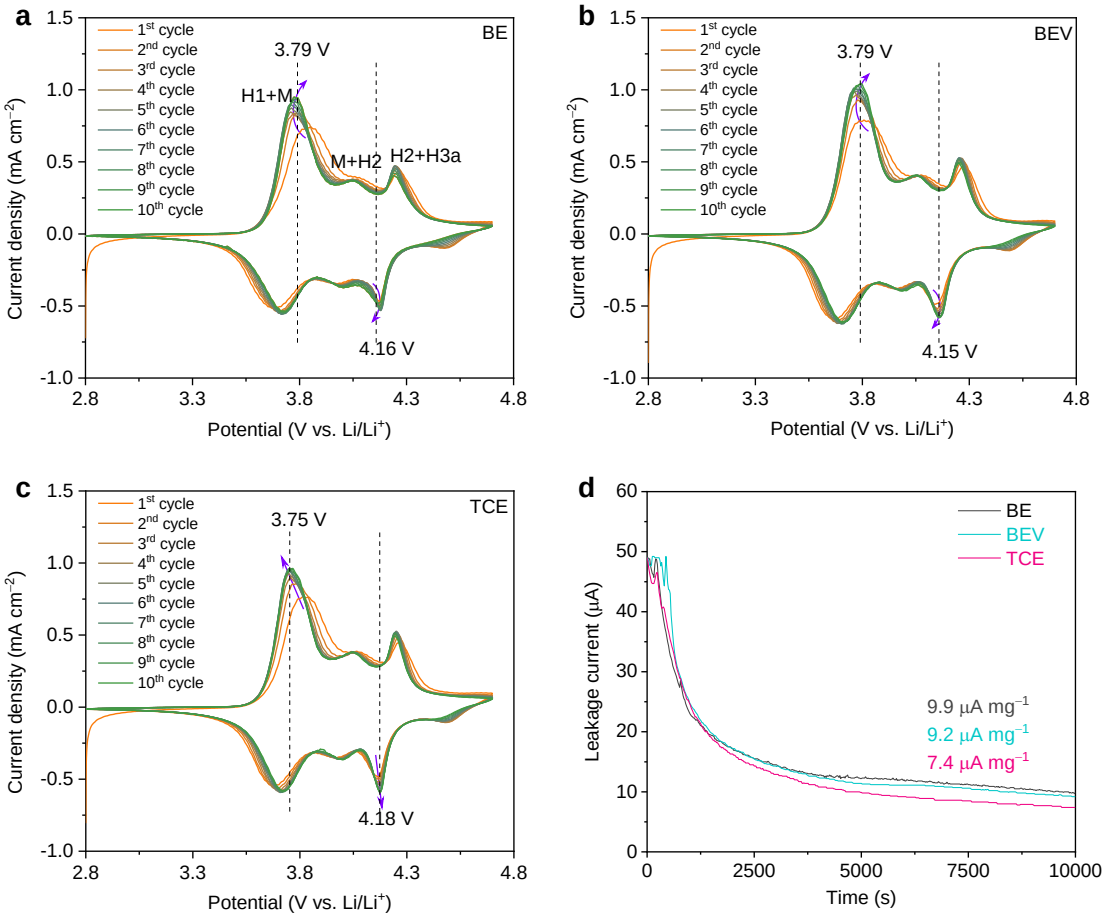

Fig. S25. CV curves of Li|NMC811 cells cycling in (a) BE, (b) BEV, and (c) TCE at 0.1 mV s^{-1}. (d) Leakage currents during 4.7 V constant-voltage floating test of the NMC811 cathodes cycled in different electrolytes.

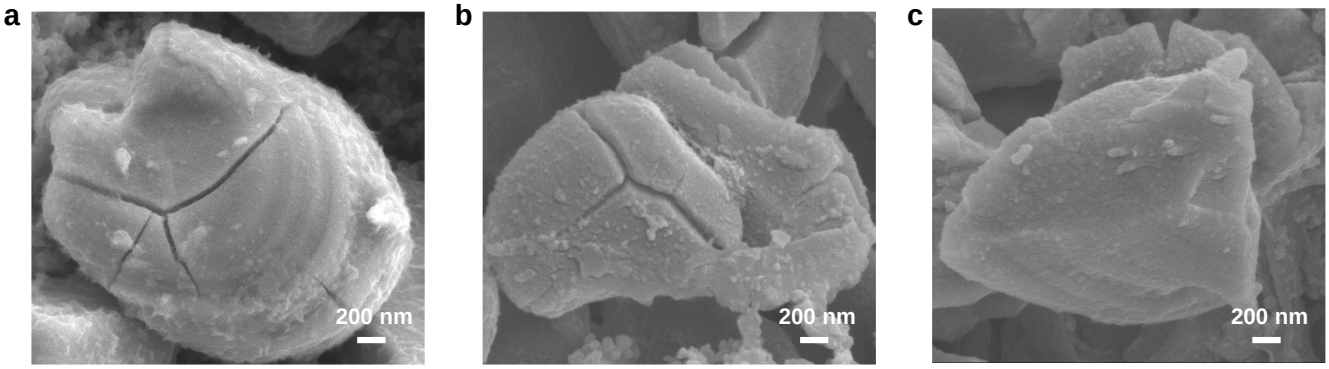

Fig. S26. Morphology of NMC811 particles cycling (200 cycles) in (a) BE, (b) BEV, and (c) TCE.

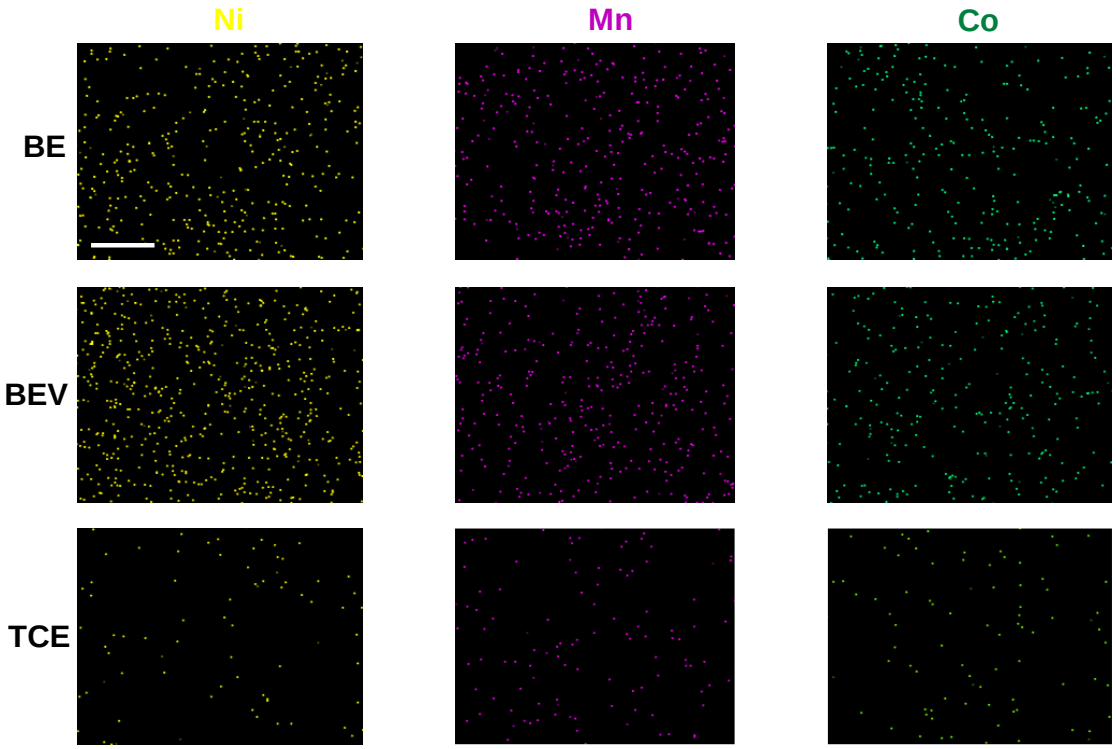

Fig. S27. EDS mapping of the lithium anodes after 200 cycles in Li|NMC811 cells at 0.5C. Scale bar: 2.5 µm.

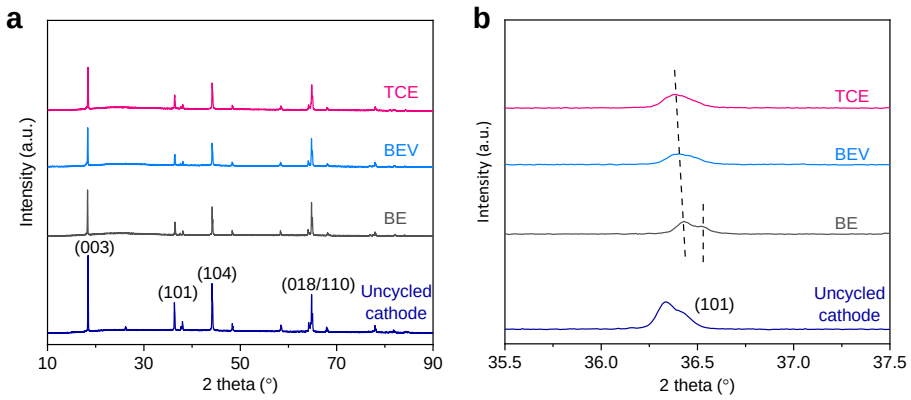

Fig. S28. XRD patterns of NMC811 cathode after 200 cycles.

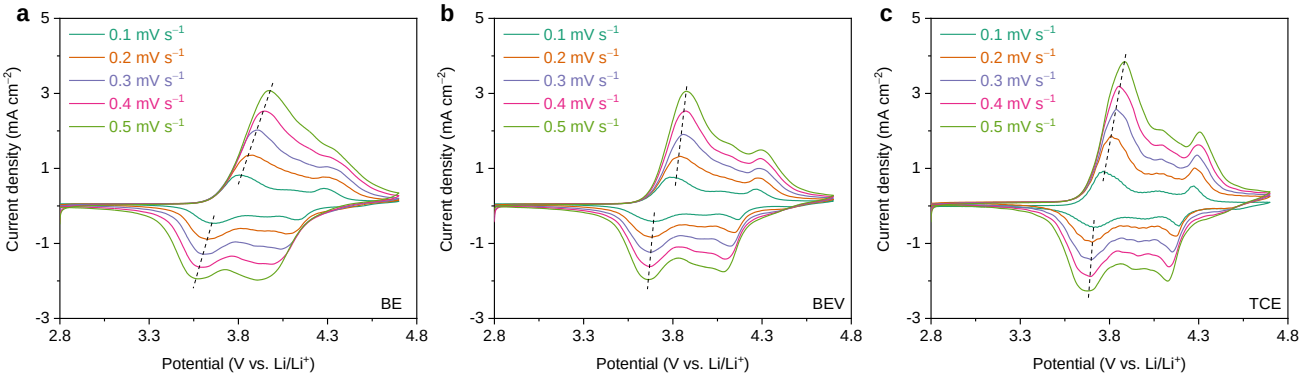

Fig. S29. CV curves of Li|NMC811 cells cycling in (a) BE, (b) BEV, and (c) TCE at 0.1~0.5 mV s^{-1}.

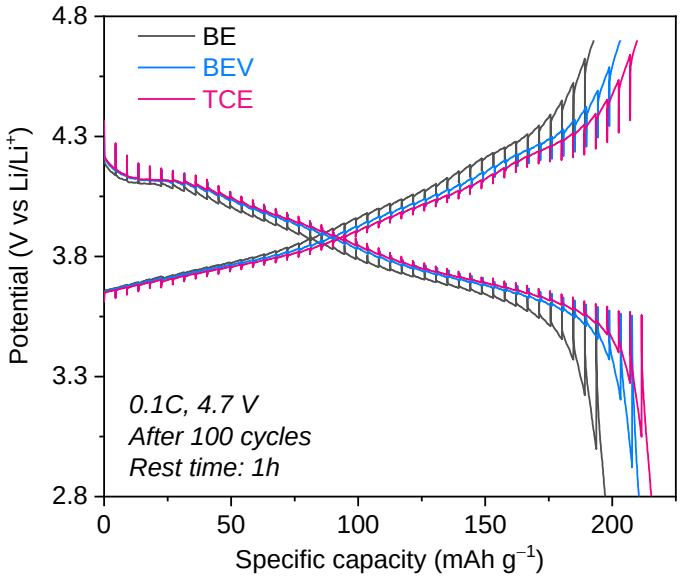

Fig. S30. The galvanostatic intermittent titration technique (GITT) potential profiles of Li|NMC811 cells.

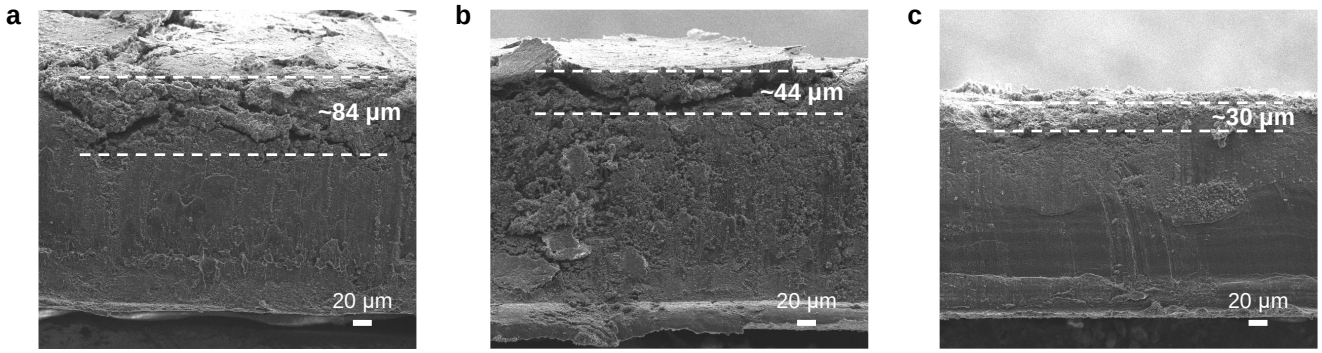

Fig. S31. Morphology of Li^0 anodes cycling (200 cycles) in (a) BE, (b) BEV, and (c) TCE.

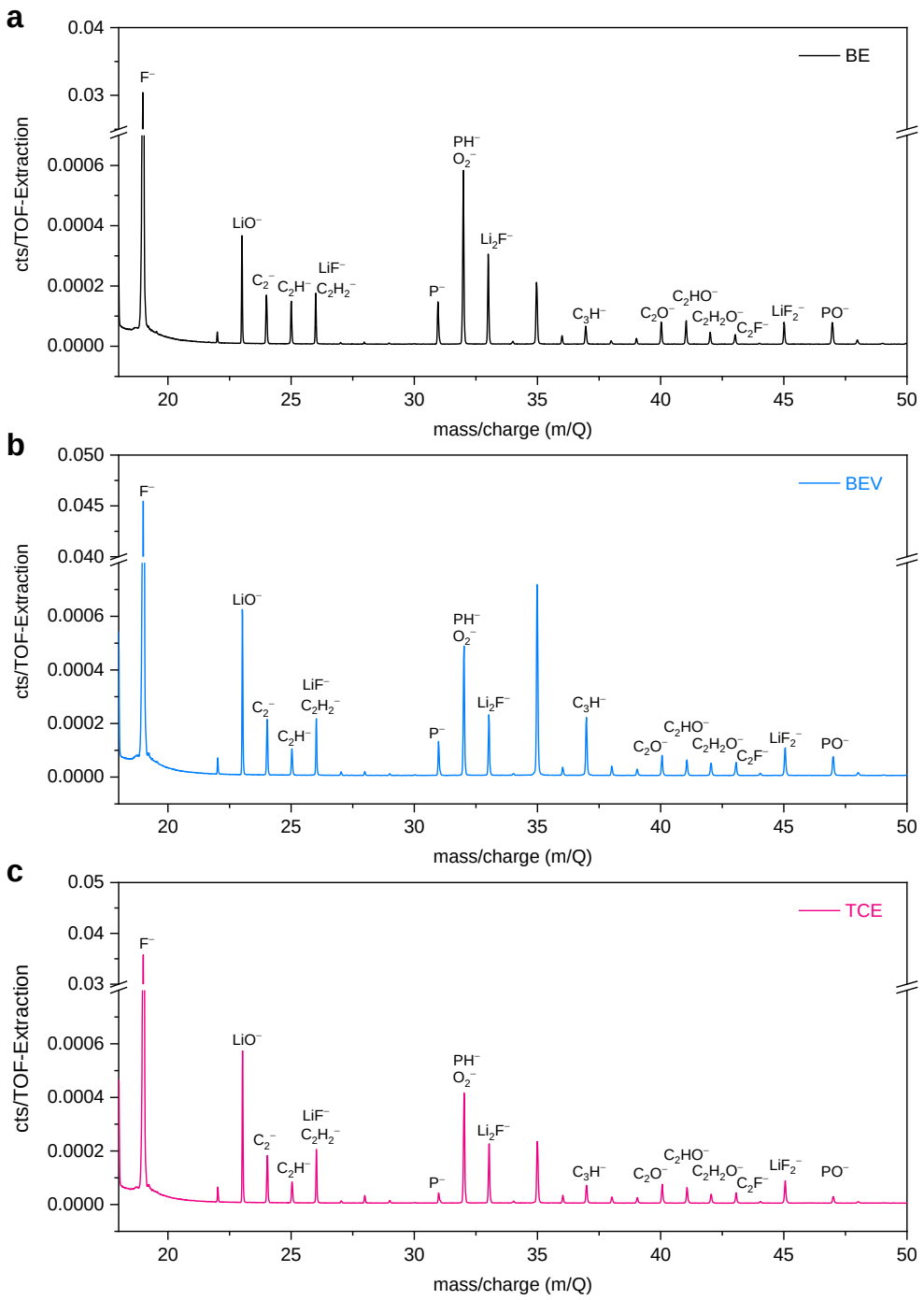

Fig. S32. Ex situ TOF-SIMS analysis of Li^0 anode retrieved from Li|Li cells with (a) BE, (b) BEV, and (c) TCE.

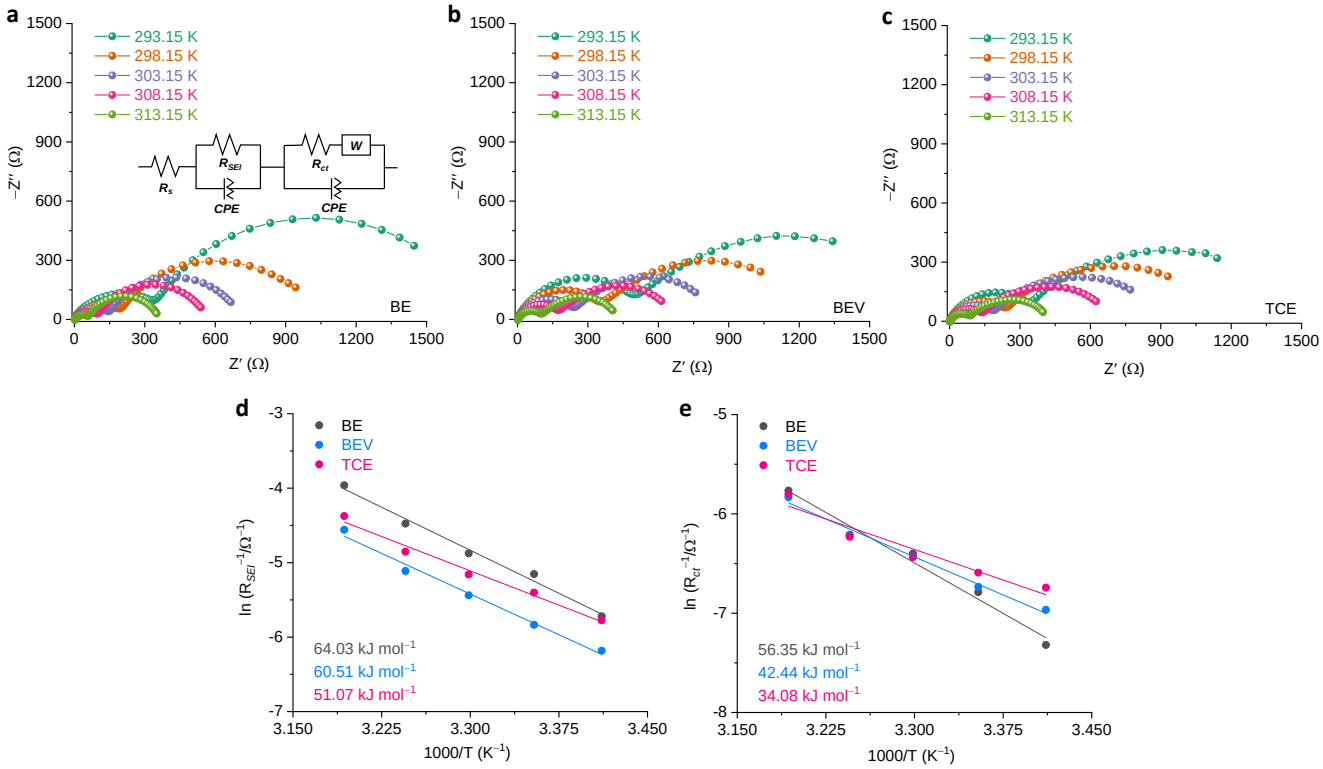

Fig. S33. Temperature-dependent EIS of Li|Li cells with (a) BE, (b) BEV, and (c) TCE. The fitting results of (d) R_{SEI} and (e) R_{ct} according Arrhenius equation.

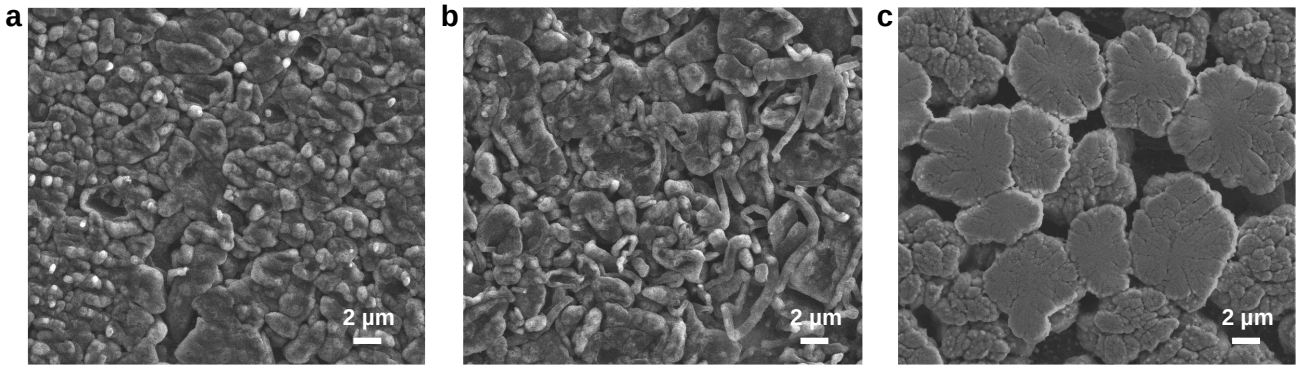

Fig. S34. Morphology of lithium metal deposited in (a) BE, (b) BEV, and (c) TCE on the Cu foil under RT.

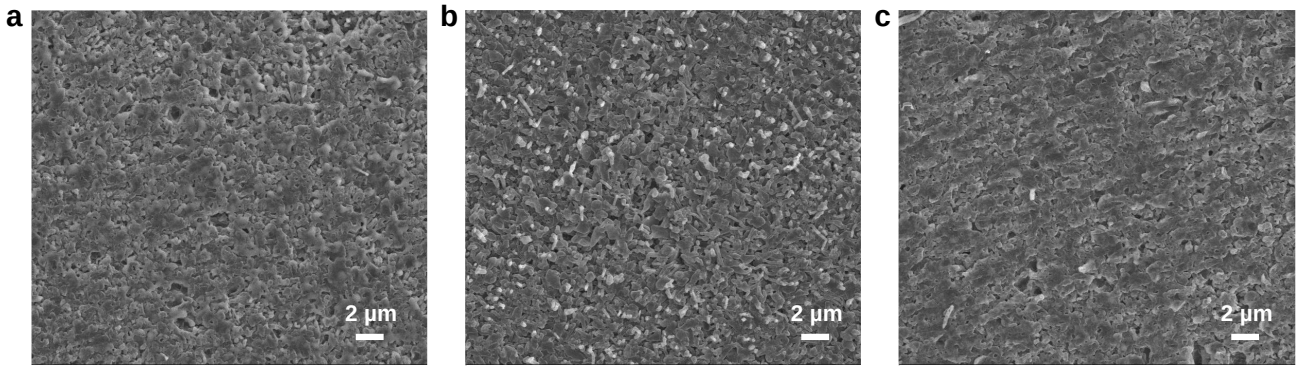

Fig. S35. Morphology of lithium metal deposited in (a) BE, (b) BEV, and (c) TCE on the Cu foil under −20°C.

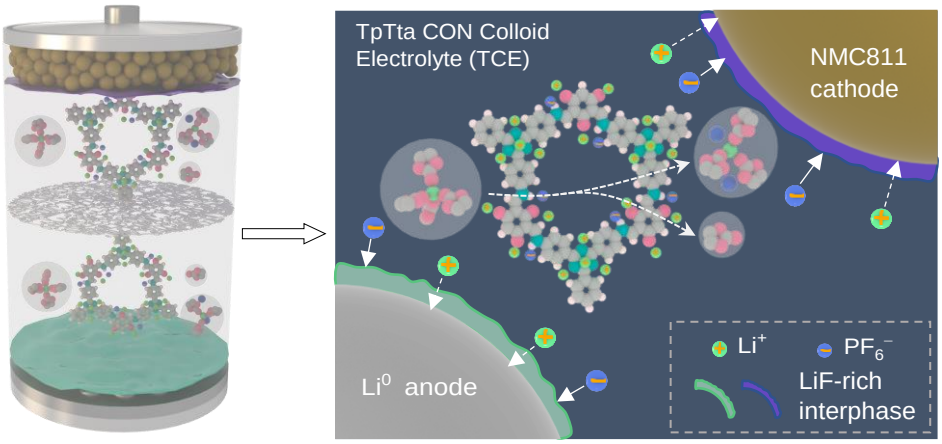

Fig. S36. Schematic illustration of the interphase evolution in the cell.

SUPPLEMENTARY TABLES

Table S1 | Atomistic coordinates of TpTta.

Lattice type: P			
Space group name: P-6			
Space group number: 174			
a:18.95070	a: 18.95070	c: 3.42950	
alpha: 90.0000	beta: 90.0000	gamma: 120.0000	
	x	y	z
N1	0.41530	0.70005	0.50000
C2	0.36698	0.61771	0.50000
C3	0.43549	0.83904	0.50000
C4	0.40170	0.89022	0.50000
C5	0.45170	0.97491	0.50000
C6	0.53731	1.01078	0.50000
C7	0.57065	0.95913	0.50000
C8	0.52063	0.87453	0.50000
N9	0.59225	1.09798	0.50000
C10	0.59150	0.43306	0.50000
C11	0.62478	0.38335	0.50000
C12	0.57665	0.29232	0.50000
O13	0.50258	0.25756	0.50000
H14	0.33628	0.86489	0.50000
H15	0.42163	1.01035	0.50000
H16	0.63608	0.98452	0.50000
H17	0.54889	0.83705	0.50000
H18	0.65328	1.11466	0.50000
H19	0.63330	0.49757	0.50000

Table S2 | A short summary of electrolyte strategies for NMC cells.

Electrolyte	Anode|cathode	Upper cut-off voltage	Tempe-rature	Current density	Initial capacity/cycle number/capacity retention	Ref.
1.0 M LiFSI / (DiFEC: MTFC: HFME, 1:2:2 vol%)+50 mM NaFSI	Gr|NMC532	4.6 V	–20℃	0.2C	139.1 mAh g^{-1} / 92 / 72.2%	*Adv. Mater.* **35**, 2210115 (2023).[25]
~5.88 M LiFSI / (EMC+TTE)	Li|NMC811	4.4 V	–20℃	C/3	155.8 mAh g^{-1} (at 100 cycles) / - / 80.7%	*Angew. Chem. Int. Ed.* **61**, 202205967 (2022).[26]
1 M $LiPF_6$ / (MP: FEC, 9:1 vol%)	Gr|NMC111	4.3 V	–20℃	0.2C	95 mAh g^{-1} / 100 / 92%	*ACS Energy Lett.* **6**, 2016–2023 (2021).[27]
1.0 M $LiPF_6$ EC/EMC/PC (4:7:1, wt%)+1 wt% $LiPO_2F_2$	Gr|NMC532	4.2 V	–20℃	0.5C	100.8 mAh g^{-1} / 100 / 91%	*Electrochim. Acta* **221**, 107–114 (2016).[28]
1 M $LiPF_6$ EC/DEC (1:1, vol%) +10 vol% FEC+7 wt% Li_2O (suspension electrolyte)	Cu|NMC811	4.3 V	RT	0.2C (charged) / 0.3C (discharged)	~3.6 mAh cm^{-1}/ 70 / ~72%	*Nat. Mater.* **21**, 445–454 (2022).[29]
TCE	Li|NMC811	4.6 V	–20℃	C/3	157.8 mAh g^{-1} / 700 / 80.7%	This work

Gr: graphite. DiFEC: trans-4,5-di-fluoroethylene carbonate. MTFC: methyl (2,2,2-trifluoroethyl) carbonate. HFME: hexafluoroisopropyl methyl ether. TTE: 1,1,2,2-tetrafluoro-3-(1,1,2,2-tetrafluoroethoxy) propane. MP: methyl propionate. $LiPO_2F_2$: lithium difluorophosphate.

Table S3 | Fitting results of three-electrode set up NMC811 cells.

	RT			−20℃		
	R_s	$R_{CEI/SEI}$	R_{ct}	R_s	$R_{CEI/SEI}$	R_{ct}
BE-cathode	2.93	98.9	606	8.27	1020	1400
BE-anode	1.71	30.5	67.1	4.08	5950	6680
TCE-cathode	2.23	64.7	240	4.22	475	1240
TCE-anode	1.41	28.2	25.5	5.15	217	4630

Unit: Ω

Table S4 | Fitting results of temperature-dependent EIS of Li|Li cells.

	BE			BEV			TCE		
Temperature(K)	R_s	R_{SEI}	R_{ct}	R_s	R_{SEI}	R_{ct}	R_s	R_{SEI}	R_{ct}
293.15	2.06	305	1510	2.76	484	1060	2.62	322	848
298.15	1.93	173	887	2.5	342	841	2.26	222	729
303.15	1.92	131	602	2.45	230	619	2.58	174	623
308.15	2.06	87.9	498	2.26	166	502	2.41	128	508
313.15	1.97	52.5	319	2.14	95.4	341	2.4	79.4	331

Unit: Ω

SUPPLEMENTARY REFERENCES

1 L. Yao, A. Rodriguez-Camargo, M. Xia, D. Mucke, R. Guntermann, Y. Liu, L. Grunenberg, A. Jimenez-Solano, S. T. Emmerling, V. Duppel, K. Sivula, T. Bein, H. Qi, U. Kaiser, M. Gratzel and B. V. Lotsch, *J. Am. Chem. Soc.*, 2022, **144**, 10291–10300.

2 M. J. Abraham, T. Murtola, R. Schulz, S. Páll, J. C. Smith, B. Hess and E. Lindahl, *SoftwareX*, 2015, **1-2**, 19–25.

3 J. Wang, R. M. Wolf, J. W. Caldwell, P. A. Kollman and D. A. Case, *J. Comput. Chem.*, 2004, **25**, 1157–1174.

4 B. Delley, *J. Chem. Phys.*, 2000, **113**, 7756–7764.

5 J. P. Perdew, K. Burke and M. Ernzerhof, *Phys. Rev. Lett.*, 1996, **77**, 3865–3868.

6 A. D. Becke, *J. Chem. Phys.*, 2014, **105**, 9982–9985.

7 S. Grimme, J. Antony, S. Ehrlich and H. Krieg, *J. Chem. Phys.*, 2010, **132**, 154104.

8 J. Andzelm, C. Kölmel and A. Klamt, *J. Chem. Phys.*, 1995, **103**, 9312–9320.

9 A. Klamt, V. Jonas, T. Burger and J. C. W. Lohrenz, *J. Phys. Chem. A*, 1998, **102**, 5074–5085.

10 Z. Piao, R. Gao, Y. Liu, G. Zhou and H. M. Cheng, *Adv. Mater.*, 2023, **35**, 2206009.

11 C. B. Jin, N. Yao, Y. Xiao, J. Xie, Z. Li, X. Chen, B. Q. Li, X. Q. Zhang, J. Q. Huang and Q. Zhang, *Adv. Mater.*, 2023, **35**, 2208340.

12 M. Winter, B. Barnett and K. Xu, *Chem. Rev.*, 2018, **118**, 11433–11456.

13 W. Li, C. X. Yang and X. P. Yan, *Chem. Commun.* , 2017, **53**, 11469–11471.

14 S. Kandambeth, A. Mallick, B. Lukose, M. V. Mane, T. Heine and R. Banerjee, *J. Am. Chem. Soc.*, 2012, **134**, 19524–19527.

15 B. P. Biswal, S. Chandra, S. Kandambeth, B. Lukose, T. Heine and R. Banerjee, *J. Am. Chem. Soc.*, 2013, **135**, 5328–5331.

16 H. Chen, H. Tu, C. Hu, Y. Liu, D. Dong, Y. Sun, Y. Dai, S. Wang, H. Qian, Z. Lin and L. Chen, *J. Am. Chem. Soc.*, 2018, **140**, 896–899.

17 S. Mitra, S. Kandambeth, B. P. Biswal, M. A. Khayum, C. K. Choudhury, M. Mehta, G. Kaur, S. Banerjee, A. Prabhune, S. Verma, S. Roy, U. K. Kharul and R. Banerjee, *J. Am. Chem. Soc.*, 2016, **138**, 2823–2828.

18 Y. Cao, M. Wang, H. Wang, C. Han, F. Pan and J. Sun, *Adv. Energy Mater.*, 2022, **12**, 2200057.

19 Y. Zheng, T. Qian, H. Ji, X. Xia, J. Liu, Y. Zhu and C. Yan, *Adv. Mater.*, 2021, **33**, 2102634.

20 X. Li, Q. Hou, W. Huang, H.-S. Xu, X. Wang, W. Yu, R. Li, K. Zhang, L. Wang, Z. Chen, K. Xie and K. P. Loh, *ACS Energy Lett.*, 2020, **5**, 3498–3506.

21 B. You, Z. Wang, F. Shen, Y. Chang, W. Peng, X. Li, H. Guo, Q. Hu, C. Deng, S. Yang, G. Yan and J. Wang, *Small Methods*, 2021, **5**, 2100234.

22 J. Sun, X. Cao, H. Yang, P. He, M. A. Dato, J. Cabana and H. Zhou, *Angew. Chem. Int. Ed.* , 2022, **61**, 202207225.

23 K. Dey, H. S. Kunjattu, A. M. Chahande and R. Banerjee, *Angew. Chem. Int. Ed.*, 2020, **59**, 1161–1165.

24 K. Dey, M. Pal, K. C. Rout, H. S. Kunjattu, A. Das, R. Mukherjee, U. K. Kharul and R. Banerjee, *J. Am. Chem. Soc.*, 2017, **139**, 13083–13091.

25 X. Zheng, Z. Cao, W. Luo, S. Weng, X. Zhang, D. Wang, Z. Zhu, H. Du, X. Wang, L. Qie, H. Zheng and Y. Huang, *Adv. Mater.*, 2023, **35**, 2210115.

26 B. Nan, L. Chen, N. D. Rodrigo, O. Borodin, N. Piao, J. Xia, T. Pollard, S. Hou, J. Zhang, X. Ji, J. Xu, X. Zhang, L. Ma, X. He, S. Liu, H. Wan, E. Hu, W. Zhang, K. Xu, X. Q. Yang, B. Lucht and C. Wang,

Angew. Chem. Int. Ed., 2022, **61**, 202205967.
27 Y.-G. Cho, M. Li, J. Holoubek, W. Li, Y. Yin, Y. S. Meng and Z. Chen, *ACS Energy Lett.*, 2021, **6**, 2016–2023.
28 B. Yang, H. Zhang, L. Yu, W. Fan and D. Huang, *Electrochim. Acta*, 2016, **221**, 107–114.
29 M. S. Kim, Z. Zhang, P. E. Rudnicki, Z. Yu, J. Wang, H. Wang, S. T. Oyakhire, Y. Chen, S. C. Kim, W. Zhang, D. T. Boyle, X. Kong, R. Xu, Z. Huang, W. Huang, S. F. Bent, L. W. Wang, J. Qin, Z. Bao and Y. Cui, *Nat. Mater.*, 2022, **21**, 445–454.